Joint Centre for Mesoscale Meteorology, Reading, UK

Mesoscale analysis of the activation of a cold front during cyclogenesis

K. A. Browning
N. M. Roberts
A. J. Illingworth

Internal Report No. 58

June 1996

Met Office Joint Centre for Mesoscale Meteorology Department of Meteorology
University of Reading PO Box 243 Reading RG6 6BB United Kingdom
Tel: +44 (0)118 931 8425 Fax: +44 (0)118 931 8791
www.metoffice.com

Designed and produced by the Met Office © Crown copyright 2001 01/0240 The Met Office logo is a registered trademark.

Submitted June 1996

Mesoscale analysis of the activation of a cold front during cyclogenesis

K A Browning*, N M Roberts and A J Illingworth

Joint Centre for Mesoscale Meteorology, University of Reading, UK

Summary

The archetypal mesoscale structure of an ana-cold front comprises a narrow cold frontal rainband (NCFR), associated with line convection, embedded within a wide cold-frontal rainband (WCFR) due to the slantwise ascent associated with a strong transverse-front mesoscale circulation. Whereas most mesoscale observational studies have concentrated on this mature stage, the present paper explores by means of a case study how such a mature frontal system developed from pre-existing features. The study is based upon the interpretation of satellite imagery, observations from conventional and multiparameter Doppler radar and surface reports, together with diagnostics from an operational mesoscale forecast model. The cold frontal zone in this case was characterized by multiple cold fronts. One of these was studied in detail from the point of view of its evolution and its relationship to neighbouring frontal bands. It started as a shallow 'rope cloud'. At a fairly early stage it produced a NCFR due to line convection. Then, over a period of only a few hours, a dry intrusion and an accompanying strong direct transverse-front circulation led to the formation of a canopy of mid-level cloud and a WCFR. The WCFR was attributable not only to the rearward-ascending outflow from the line convection but also to the reinvigoration of ascent at an earlier cold-frontal zone that it was undercutting. Although this transverse circulation was probably intensified by precipitation processes, it is inferred that it was mainly a

*Corresponding address: Joint Centre for Mesoscale Meteorology, Harry Pitt Building, University of Reading, Whiteknights Road, PO Box 240, Reading RG6 6FN, UK. (The Joint Centre for Mesoscale Meteorology is supported by the Meteorological Office and the Department of Meteorology, University of Reading).

manifestation of the larger-scale environmental flow that existed independently of the major precipitation features.

1. Introduction

Figure 1 is an adaptation of the frontal-fracture stage of Shapiro and Keysers' (1990) model of a developing cyclone to represent a typical frontal cyclone affecting NW Europe. It shows the frontal analysis in relation to system-relative flows and cloud features as described in the caption. The Figure shows four cold-frontal regions (the fronts being defined in terms of wet-bulb potential temperature, θ_w): Two of these regions, ie along ab and part of cd, are sharp cold fronts often characterised by line convection. The region between b and c corresponds to a diffuse surface frontal zone. The fourth region, between b and d, corresponds to an upper cold front. The studies of NW European cyclones summarized by Browning (1996) have clarified the relationship of these fronts to the patterns of airflow, cloud and precipitation. What is less clear, however, is the detailed manner in which the cold fronts evolve in getting to the stage depicted in Figure 1. The broad-scale evolution in the frontal structure described by Shapiro and Keyser is evident, but the mesoscale evolution of the fronts, and in particular the patterns of cloud and precipitation, are not. The observational and mesoscale-model based diagnostic study in the present paper addresses these issues.

Our objective, to describe the evolution of the cold-frontal cloud and precipitation structure, might seem a fairly simple one; however, in practise such frontal regions tend to be complicated by multiple structure upstream in the approaching cold air and it is not always

easy to keep track of individual components of the resulting substructure. It is perhaps because of this that studies of frontal evolution often rely more heavily on model simulations than on observations. Here we shall rely on the observations rather more than on the model, although both are indispensible. Some insight into the nature of this multiple structure has already been gained from IOP3 of the FRONTS 92 experiment in which a dense array of dropwindsondes was released over the sea during the early stages of cyclogenesis. An analysis of the IOP3 fronts revealed two levels of fine structure (Browning et al 1995): there were two distinct cold fronts about 100 to 200 km apart plus some secondary structure on a smaller scale. The primary fronts were associated with two distinct regions of dry, low-θ_w air ('dry intrusions'). These dry intrusions descended from the upper troposphere and were trackable in satellite water vapour imagery as 'dark zones'. The two primary cold fronts appeared as surface features producing thin lines of shallow cloud early in the process of cyclogenesis, but the subsequent evolution of individual fronts was not well resolved on the mesoscale.

In the present case, the cyclogenesis took place close to the British Isles and so, for much of the time when the fronts were producing precipitation, they were within range of the land-based weather radar and conventional observational networks. These, along with Meteosat imagery, revealed the development of multiple fronts which were sharp in places, one of them developing line convection. This was confirmed by detailed Doppler measurements from the research radar at Chilbolton which provided an important observational component of this study. Other parts of the fronts were shown to be less sharp and in some places the evidence from the Met Office's operational mesoscale model showed

that they became purely upper fronts. Together with the multiple-front structure, this kind of variability, in both space and time, makes mesoscale analysis a challenging task.

This case, in having multiple cold-frontal structure, was similar not only to the FRONTS 92 IOP-3 case but also to several others we have studied superficially. We believe on the basis of these unpublished studies that such multiple (2 or more) structures are very common. This would also be consistent with the multiple rainband structure that typifies the later stages of cyclone evolution (Kreitzberg and Brown 1970 and many later studies, eg Saarikivi and Puhakka 1990). In the present study, we describe the evolution of one of the fronts in particular detail as it was activated from an initially shallow rope-like cloud eventually to become very sharp at the surface, with line convection and heavy precipitation in one part, and an upper cold front, with no surface front but still heavy precipitation, in another part. We also show that, as it intensified, this front interacted with another cold front ahead of it. For more accurate very-short-range forecasts to be made it will be necessary to understand these associated mesoscale processes and to ensure they are properly represented within numerical weather prediction models.

The hydrostatic operational mesoscale model that we use as a diagnostic tool reproduced some key features of these fronts but it also failed in important respects, notably in not representing the mesoscale transverse circulation and the line convection that was embedded within it. In general, these features produce significant weather and so their accurate prediction is of more than academic interest. Although this is not the main purpose of the paper, our analysis sheds some light on the possible reasons for the failure in the model.

2. Synoptic-scale overview

The synoptic setting for the present case study is summarized in Figure 2. The model used in the rest of this study is the mesoscale version of the Met Office Unified Model but, first, to provide the large-scale context we use the Limited Area (LAM) version of the same model. Shown in Figure 2 is the msl pressure analysis from the LAM superimposed upon the Meteosat infrared imagery at 6-hour intervals starting at 06 UTC on 24 October 1995. The initial time shown (Fig 2(a)) is early in the development of the cyclone of interest which formed a closed circulation several hours later over Ireland (Fig 2(b)). The model-derived msl pressure at 06 UTC in the area of the incipient cyclone was 991 mb, dropping to 985 mb by 12 UTC. Observed central pressures decreased from 984 mb at 13 UTC when the closed surface low was first observed to 974 mb at 19 UTC as the new centre travelled northwards at about 100 km h^{-1} from a location 200 km south of Ireland to the north coast of Ireland. By 00 UTC, 25 October, it had reached the Hebrides with a central pressure of 965 mb (968 mb in the model, Fig 2(d)).

The dominant cloud features in Figure 2(a) are the swirl of cloud associated with the primary cyclone near 25°W 58°N and a long polar-front cloud band (PFCB) associated with a cold front, referred to as Cold Front I (CF I), which at 06 UTC was extending from west of Portugal across western Ireland to Iceland. The cloud features that formed in association with the secondary cyclone (L) analysed in this paper can be seen developing to the west of the PFCB initially as two mesoscale cloud areas, labelled II and III (Fig 2(a)). As they developed, II and III merged and acquired a more sharply defined cloud structure corresponding to the feature C in Figure 5.2.11-13 of Bader et al (1995). This is the

developing cloud head described by Browning and Roberts (1994), Bader et al (1995) and others. As is clear from the full-resolution imagery (shown later), cloud features II and III occurred at the northern end of shallow and often rope-like cloud lines. Continuity with later measurements shows that these corresponded to surface cold fronts. The case study deals in detail with the evolution of the cold front connected with cloud area II and more briefly with cold fronts I and III. At the time corresponding to Figure 2(a), there was little interaction between CF II and the PFCB associated with the old cold front (CF I). During the next 12 hours, however, CF II merged with the PFCB, and the CF I itself frontolysed, at least at low levels. The entire process conformed to the instant occlusion process as described by Zillman and Price (1972), McGinnigle et al (1988) and Bader et al (1995) - see, in particular, McGinnigle et al's model in their Figure 14. The main difference was the existence of the multiplicity of cold frontal structure in the present case.

3. Mesoscale analysis of the satellite and radar imagery

3.1 Overview of the multiple cold-frontal structure

Figure 3 shows a frontal analysis for 15 UTC, based on imagery, some surface observations and model output, to provide a context for the detailed mesoanalyses presented in this section. Aspects of the analysis are justified later. The analysis time corresponds to the onset of the mature phase of what became the dominant cold front (CF II). CF II is discussed in Section 3.2. Several other cold fronts are shown behind it. Two of these were evanescent; the others, CF III and IV, were long-lived. CF III is discussed in Section 3.4. Ahead of the main cold front (II), CF I was in the process of frontolysing; this front is discussed in Section 3.3. CF I had earlier been responsible for the original polar-front cloud

band (PFCB) ahead of the developing cloud heads II and III which are shown in Figure 3 at the northern ends of the corresponding cold fronts. Early in their development, and throughout their development in places close to the cold fronts, the cloud heads were characterized by convective cloud. As they grew and matured, the cloud heads became increasingly composed of stratiform cloud.

3.2 Evolution of cloud and precipitation associated with Cold Front II

(a) The early stage (<12 UTC)

In the early stages of CF II, between 07 and 12 UTC, it was well-observed over the sea by Meteosat. It appeared as a rope cloud (Scorer 1986, Bader et al 1995), particularly distinctive in the visible imagery (Figure 4(a)). We have no in situ measurements over the sea in the present study. However, detailed in situ measurements during the passage of similar rope clouds reported in the literature show that they are associated with cold fronts with abrupt wind shifts, temperature drops and pressure jumps concentrated within a strip of order 1 km wide. Observations of rope clouds in Australia (Smith et al 1995) show that typically such fronts are shallow (~ 1 km deep) and dry (ie non-precipitating). Observations in the USA (Shapiro et al 1985, Shapiro and Keyser 1990) show that, although they may be dry and shallow, vertical velocities of up to 5 m s^{-1} can nevertheless occur. Infrared imagery (Figure 4(b)) showed that the cloud tops in the present case were between +5 and 0°C, corresponding to a height of only 2 to 3 km. A series of tracings of the rope axis and other associated cloud features during this period is shown in the left-hand half of Figure 5. The more complete 09 UTC tracing in Figure 5 shows that the rope cloud at its northern end

extended into the developing cloud head in which cloud-top temperatures were as low as -40 to -50°C.

Individual plumes of cold cloud, with tops intermediate in height between those of the rope and cloud heads, appeared to originate from sources along the rope cloud; Figure 5 shows these streaming away towards the north, rearwards at an angle of 30 deg to the rope cloud. The tops of these cloud plumes in some cases rose with distance downwind of their sources rather than having a maximum height at the source. This suggests that the plumes may have been due to boundary-layer air rising slantwise as laminae of ana-cold frontal ascent as described in Browning (1995), rather than as anvil plumes emanating from the tops of convective cells along the cold front.

(b) Transition towards mature stage (12-14 UTC)

At 12 UTC, upper cloud associated with CF I which was starting to rejuvenate (see Section 3.3 later), began to obscure the CF II rope cloud as it caught up with CF I. However, it was at about this stage that the northern end of CF II came within clear view of the land-based radars and the corresponding radar-derived frontal positions are shown in the right-hand part of Figure 5 (and in the inset to Figure 5). We now examine the precipitation and cloud structure as CF II came within view of the Cornwall weather radar in southwest England (Figure 6).

Figure 6 (a, b, c) shows the narrow cold-frontal rainband associated with CF II approaching southwest England. It can be seen to have been embedded within an extensive

and rapidly developing region of lighter precipitation. The narrow cold-frontal rainband evolved from a line of small cells of moderately heavy rain at 12 UTC (Figure 6(a)) to a thinner line of moderately heavy rain, parts of which were sufficiently 2-dimensional to be consistent with line convection (see b and c). The corresponding Meteosat IR pictures in Figures 6 (d, e, f) show that parts of the line convection echo for some of the time were embedded within moderately deep cloud with tops occasionally colder than -28°C; but there was no consistent relationship between the cold clouds and the line convection and, indeed, the convection responsible for the thin line of most intense radar echo is believed to have been much shallower. Line convection in the UK is seldom much deeper than 3 km and it was certainly no higher than this several hours later when it was within range of the vertically-scanning Chilbolton radar (Section 5). However, the only observational evidence for the line convection being as shallow as this at an early stage is the fact that part of the corresponding echo (see southern part of line in Figure 6(b) between 150 and 200km range from the Cornwall radar) was associated with a portion of rope cloud with tops below 4.5 km (-10°C) that could be glimpsed in the gap between areas of higher (colder) cloud (Figure 6(e)).

The ragged areas of upper-level (rather cold) cloud identified by the small circles labelled A, B, C and D in Figure 6 (d, e, f) were travelling northwards as they were undercut by CF II coming from the southwest. They can be seen getting deeper (colder) as they travelled northwards. They were also growing in horizontal extent, and were associated with the rapid increase in coverage of rain echoes surrounding the line convection between 12 UTC (Figure 6(a)) and 14 UTC (Figure 6(c)). They were related to CF I and we shall return to this topic in Section 3.3.

(c) Mature stage

Analysis of successive radar pictures shows that CF II continued to travel northeastwards as shown in the right-hand part of Figure 5 and in the Inset. By 18 UTC, the radar network picture in Figure 7 shows a narrow band of heavy rain embedded within a 150-km wide band of light-to-moderate rain. These are archetypal examples of the narrow and wide cold-frontal rainbands (NCFR and WCFR) in the classification of Houze et al (1976). The WCFR extended from France to Scotland but the NCFR extended only between latitudes 49°N and 53°N. Data in Sections 4 and 5 confirm that the latter was indeed line convection associated with a sharp surface cold front. The portions of CF II drawn boldly in Figure 5 show the radar-derived extent of this line convection at different times. To the north of the line convection, over the Irish Sea and eastern Ireland, the positions of CF II in Figure 5 have been inferred by radar from the locus of more scattered outbreaks of convective precipitation. Here the cold front was no longer a surface feature; rather, as shown in Section 4, it was an upper cold front. The WCFR was the result of rearward-ascending slantwise ascent, typical of an ana-cold front. We show later (Section 5) that it was due partly to outflow from the CF II line convection itself and partly to the ascent of moist air associated with the old CF I (Section 3.3).

3.3 Evolution of cloud associated with Cold Front I

The ragged areas of higher (colder) cloud, A, B, C and D, seen developing in Figure 6 (d, e, f) were amongst a number of fairly regularly spaced areas of rather high cloud

associated with CF I. Figure 8 shows that they continued to grow in horizontal and vertical extent to form the mesoscale plumes that so dominated the infrared imagery at the later times. Their growth during this period appeared to be occurring in association with the same belt of mesoscale ascent that was responsible for the increasing vigour of CF II which was then undercutting them.

Figure 9 shows that the mesoscale cloud plumes identified in Figs 6 and 8 developed from the residues of previous strongly convective areas of cloud that could be traced from 01 UTC (and earlier) when the PFCB associated with CF I had been intense. Sferics observations showed that the cloud area that developed into Plume C, for example, had been a thunderstorm within the PFCB at 01 UTC. At this time it was producing a forward-trailing anvil and was located at 41½°N 14°W. The *forward*-trailing behaviour of this, and the other similar, anvils is consistent with an overrunning kata-cold frontal circulation characterising CF I as it underwent frontolysis. By 09 UTC, storm areas C, D and E, along with their neighbours along the PFCB, had almost entirely decayed. But then, from 11 UTC onwards, as shown by Figures 6 and 8, these areas of cloud and others like them along the old frontolysed CF I, began to develop into the mesoscale plumes which this time were trailing *rearwards* in association with what was evidently a newly developing ana-cold frontal (ie direct) circulation. These rearward-trailing plumes were shallow at first with tops below 5 km but, as the ana-circulation became established, they steadily deepened to 8 km (Figure 8).

We interpret the plumes A-E as being due to air, moistened by the evaporation of the anvil residues from earlier convection along CF I, coming under the influence of a band of

renewed synoptically-forced ascent which was invigorating both them and the CF II line convection. The purpose of this paper is to describe the evolving response of small-scale cloud and precipitation events to changing larger-scale forcing; it is beyond the scope of the paper to diagnose the cause of the change from kata- to ana-circulation in this region other than to say that its onset preceded and was presumably independent of the generation of mesoscale rearward-sloping outflow from the line convection, discussed next.

Figure 8(c) shows that at 17 UTC the upper-level plumes were superimposed upon a wide band of middle-level cloud, with background tops at about 5 km (-10°C) (fairly dark grey), that was by then completely enveloping the line convection and was due in large measure to it (cf Section 5). Two hours later, at the time of the Doppler radar measurements in Section 5. the tops of this background cloud canopy had risen to 5.5 km (-15°C) whilst the tops of the mesoscale plumes remained at 8 km (over southern England). Evidence in Section 5 shows that the CF I plumes were situated just above the region of cloudy slantwise ascent that was being generated by the outflow from the CF II line convection. The demarcation between cloud due to CF I and CF II cannot be determined precisely but the later analysis suggests that from 18 to 19 UTC it occurred between 5 and 7 km. By 1830 UTC the WCFR had become fairly 2-dimensional. However, prior to this, the WCFR had been distinctly non-2-dimensional and, indeed, at 16 and 17 UTC, Figure 8 shows that the pattern of rainfall within the WCFR bore the clear imprint of the CF I cloud plumes shown by Meteosat. Evidently, therefore, the rainfall in the WCFR at this time was being strongly influenced by CF I. The more uniform pattern of rainfall at 18 and 1830 UTC (AMS 1996) shows that the WCFR eventually became dominated by the more nearly 2-dimensional rearward-sloping outflow from the CF II line convection.

3.4 Evolution of cloud and precipitation associated with Cold Front III

Successive hourly positions of Cold Front III as inferred from imagery between 13 and 21 UTC are sketched in Figure 10. This front behaved similarly in some respects to CF II. The main difference was that part of CF III developed a minor wave. This amplified between 15 and 17 UTC but then collapsed by 20 UTC, although the associated rain did not diminish. Rain was confined to a narrow strip along the surface cold front, except for that beneath the plumes of cloud that extended rearwards of the surface front to compose the southern tip of Cloud Head III. These plumes occurred over a 100 km segment of CF III near and just to the north of the tip of the wave -see the patterns of rain and cloud in Figures 7 and 10.

4. Mesoscale analyses of the dynamic and thermodynamic structure of the cold fronts

4.1 Mesoscale model analyses

Figure 11 shows analyses for 18 UTC, at a time when the model would have been benefiting from land-based surface and upper-air observations representing the detailed frontal structure. The figure shows θ_w - analyses at (a) 850 mb and (b) 650 mb and the corresponding relative humidity analyses at these two levels (c and d). Also marked are an upper cold front and two sharp surface fronts produced by frontal fracture as in Figure 1. One of the sharp surface fronts in Fig. 11 is an almost stationary warm front extending down the west coast of Scotland to the centre of the surface low (L) and terminating as a bent-back front near southeast Ireland. The other front, extending from Britanny northwards to

southwest Scotland, corresponds to CF II. This is analysed on the basis of the radar and surface data (see later) as a sharp surface feature (solid cold-front symbols) over much of its length but as an upper feature only (open symbols) north of the point where it crosses into the Irish Sea. This is seen to be consistent with the model-derived θ_w-pattern which shows the front to be situated at the leading edge of the θ_w-gradient all along its length at 650 mb (Figure 11(b)) whereas at 850 mb the leading edge of the θ_w-gradient appears to be holding back along the north Wales coast (X in Figure 11(a)) reminiscent of the schematic in Figure 1. The other cold fronts diagnosed in Section 3 are not marked in Figure 11: CF I had frontoloysed by this time, whilst CF III and CF IV, still further behind, may have been associated with the (ill-defined)regions of tightened gradient close to the 11.5 and 8.5°C contours in Figure 11(a).

The dry air shown in Figure 11(c and d) digging in behind CF II is regarded as being a key feature in the analysis. This is the 'dry intrusion'. Appropriate vertical sections (not illustrated) show that in the region of the Irish Sea, behind the CF II upper cold front and just ahead of the bent-back front, the dry-intrusion air at 650 mb (see long arrow in Fig 11(d)) was overrunning a moist zone within which relatively warm moist air (corresponding to the W2 flow in Fig. 1) extended from the surface up to about 750 mb. Farther south, a finger of dry-intrusion air can be seen at the 850-mb level (see long arrow in Fig 11(c)) extending northwards across southwest England just behind the surface frontal position of CF II. A vertical section along the axis of this finger, plotted in Figure 12(d), shows it entering at low levels from southwest of Britanny. The sequence of 850 mb diagrams in Figure 12(a, b and c) shows a consistently close relationship between the dry-intrusion finger and the sharp surface cold front as CF II developed from 12 to 18 UTC. Observational evidence presented

later shows that the dry-intrusion finger was the forward-directed part of a strong mesoscale circulation transverse to the cold front. We shall be arguing that this dry-intrusion finger played a role in driving the line convection that was occurring along CF II.

Further insight into the nature of this dry finger is provided by the west-east section across it in Figure 13. The relative humidity pattern in Figure 13(a) shows that the finger of dry air was situated just behind and beneath the rearward-sloping base of the canopy of moist air (shaded region up to about 350 mb) part of which was producing the WCFR associated with CF II and the residues of CF I. The vertical arrow extending up to almost 700 mb in Figures 13(a-d) represents the observationally-determined position and extent of the CF II line convection. This was pumping up boundary-layer air with a model-derived θ_w of 14.5°C (Figure 13(b)) associated with strong low-level winds which exceeded 25 m s^{-1} at 850 mb (Figure 13(c)). Later we shall show that there were much sharper changes in wind and temperature across the line convection than shown by the model. We shall be attributing the poor model performance in this regard to factors that prevented air in the model's dry finger from penetrating to the ground and advancing as a density current behind CF II. We shall show that part of the problem lies in the weakness of the model's transverse circulation in the vicinity of CF II (Figure 13(d)). The Doppler radar observations presented later (Figure 16) reveal a strong component of relative flow approaching the front within the dry intrusion which the model failed to reproduce.

Figure 13(a) shows another, shallower, canopy of moist air (shaded), extending up to about 650 mb just behind the dry finger discussed above. This was related to CF III which, according to Figure 7, was generating a region of moderate stratiform rain between 4½°W and

7°W. The canopy of moist air associated with CF III can be seen in Figure 11(d) reaching the 650-mb level over extreme southwest England. At lower levels (Figure 11(c)) it was more extensive and occupied a large fraction of what otherwise would have been a broad dry intrusion.

4.2 Surface observational analyses

The msl pressure analysis for 18 UTC is shown in Figure 14, together with a frontal analysis and a schematic portrayal of the high-θ_w surface flows (warm-conveyor- belt flows) ahead of CF II and CF III. The frontal analyses are consistent with those derived from the imagery, the model and with reports from surface stations. Over most of England the main front, CF II, produced a sharp pressure kick as shown by Stations M and S in Figure 15(a). Farther north, however, where the front is diagnosed as a purely upper cold front, Station R shows no such pressure jump in association with the passage of CF II. The high-θ_w surface air in Figure 14 is seen to have remained ahead of CF II over southern and central England where the latter is analysed as a surface cold front. But, to the north of this, it flowed rearwards underneath CF II where it is analysed as an upper cold front, before finally ascending at the bent-back front close to the low centre. Air within the high-θ_w surface flow just ahead of the surface cold front over England also had a rearward component relative to the advancing front within the frictionally-backed lowest kilometre, but this ascended as line convection at the cold front (see Section 5) rather than flowing beneath it. This is consistent with the abrupt veer in the surface wind at stations such as M in Figure 15(b) and is in contrast to the lack of a corresponding veer at the northern station R.

Just behind the CF II line convection, Figure 14 shows a strip of lower-θ_w air (10-12°C). It is separated from the main push of cold air behind CF III by a resurgence of (slightly) higher-θ_w air due to warm advection just ahead of CF III. This strip of lower-θ_w air is about 400 km long and 100 km wide, and is attributable to cold air brought down to the surface within a descending circulation behind CF II. The observed θ_w is 1-2°C colder than that at the surface as given by the mesoscale model. One has to go above 950 mb and 200 km further west to find a correspondingly low value of θ_w in Figure 13(b). This shortcoming of the model is consistent with it underestimating the transverse frontal circulation (as confirmed in Section 5).

The strip of lower-θ_w surface air just behind CF II was observed to elongate with time from 17 to 20 UTC (not shown), in line with the growing north-south extent of the CF II line convection during this period. This is, however, in contrast to the model-derived evolution which, although depicting a northward displacement of the finger between 12 and 15 UTC (Figures 12(a) and (b)), showed no more northward displacement at 18 UTC. This is a further indication of the model's failure to reproduce the correct mesoscale behaviour of the dry-intrusion finger.

5. Observations of CF II from the Chilbolton radar

The high-power multiparameter Doppler radar at Chilbolton was being operated as part of the HYREX (Hydrological Radar Experiment) during the passage of the belt of rain associated with CF II. It was operated in a sequence of RHI (Range Height Indicator) scans roughly at right angles to the front, interspersed with PPI (Plan Position Indicator) scans over

a 90-deg sector. We shall present data from 2 RHI scans to reveal the nature and true sharpness of CF II during its mature stage.

5.1 Transverse circulation at CF II

Figures 16 (a and b) show radar information obtained from an RHI scan along 268°. at right angles to the approaching cold front CF II at 1839 UTC: (a) shows almost the full width of the associated WCFR whereas (b) focuses on the portion close to the embedded NCFR (line convection). The grey shades, giving the pattern of radial Doppler velocity, draw attention to the pronounced region of horizontal convergence below 1.5 km and divergence above 1.5 km at the location of the line convection (26 km range). This is difficult to visualise in a monochrome presentation and the interested reader is referred to AMS (1996) for a colour version of this velocity display. Except close to the radar, in a relatively uninteresting region at upper levels, these radial velocities are a good approximation of the transverse-front velocities, from which it has been possible to derive the streamline pattern in Figure 16(a) assuming 2-dimensional flow.

The streamlines in Figure 16(a) show 3 main flows, drawn relative to the motion (left to right) of CF II:

'Flow 1' - This is the main precipitation-producing flow due to high-θ_w air originating in the boundary layer ahead of the front. The associated streamlines show the

boundary-layer air travelling from right to left and being lifted rapidly through 2 to 3 km before ascending gently to produce the 80-km wide region of light-to-moderate precipitation behind the surface front (the WCFR ended just beyond the 95-km range of the display). Over a zone ½ to 1 km wide in the line convection, at a height of 1 to 2½ km, the updraught velocities are calculated to have been over 15 m s^{-1} although this may be overestimated somewhat owing to inadequacy of the 2-d assumption. Within the slantwise portion, in the region of strongest (>10 m s^{-1}) rearward flow (dark shading between the 3 and 5-km levels), the streamlines can be seen to rise 2 km over a distance of 65 km, corresponding to a mean updraught of 30 cm s^{-1}. Again, this is subject to some overestimation, owing to the 2-d steady-state assumption but there was clearly an extensive region with substantial stratiform ascent.

'Flow 2' - This is the rear-to-front (RTF) flow of cold air that was catching up (from left to right) with CF II at low levels. These streamlines start off within the darkly shaded layer at and just below 2 km but then they mostly ascend and travel rearwards at the base of 'Flow 1' probably contributing to further growth of the precipitation falling from 'Flow 1'. The strength of the RTF inflow puts it into the "strong rear inflow" category as defined by Smull and Houze (1987). The fact that the inflow velocity of 12.5 m s^{-1} found at the trailing edge of the WCFR decreased towards the surface cold front suggests that the RTF inflow was driven more by the environmental flow than by the internal dynamics due to precipitation. Nevertheless, as suggested by Yang and Houze (1995), the microphysics and especially the evaporative cooling are likely to have been important in maintaining the observed fairly strong RTF inflow all the way to the position of the surface cold front.

'Flow 3' - This is the region ahead of the line convection (ie close to the radar), between a height of 1 and 5 km, which has a very small relative velocity (rather pale shading). It corresponds to the part of the warm-conveyor-belt flow above its frictionally-turned 'Flow 1' portion. According to Figure 13(c), it has a strong (>25 m s^{-1}) parallel-front component.

In addition there was another region, **'Flow 4'**, which was more clearly evident in RHI scans for other times (not shown). This was a rearward flow similar to 'Flow 1' but situated above it at times when the mesoscale plumes associated with CF I (see Section 3.3) were encountered within the Chilbolton radar cross-section. 'Flow 4' was characterised by a typically 2 to 5 m s^{-1} rearward component within patches of weak precipitation echo at heights between 6 and 8, and occasionally 9 km. Probably some of the flow between 5 and 6 km in Figure 16(a) can also be attributed to 'Flow 4' since the limitations in the 2-d assumption would most likely imply that the uppermost streamlines due to 'Flow 1' should be at a rather lower level than shown.

The nature of the flow in the immediate vicinity of the line convection, ie the surface front, is revealed more clearly by the expanded scales used in Figure 16(b). The shading in this diagram refers to quantities discussed in Section 5.2; for the moment we continue focusing on the streamlines which are depicted here at closer intervals than in Figure 16(a). As in the cases studied by Carbone (1982), Hobbs and Persson (1982) and Parsons (1992), the flow of cold air at low levels behind the surface front ('Flow 2') has some of the hallmarks of a density current: Firstly, the flow is catching up the surface front; forward relative velocities in excess of 2 m s^{-1} occur over a depth of 1 km centred at a height of 1 km.

Secondly, the depth of the forward flow tends to increase within a 'head'-like region 5 km behind the surface front; the lower part of the flow descends and flows rearwards in a shallow frictionally-retarded undercurrent while the upper part rises eventually to flow parallel to the overriding 'Flow 1'. And, thirdly, in the 'head' region there is evidence of waves or eddies of wavelength 2 or 3 km which may be due to the Kelvin-Helmholtz shearing instabilities that can be expected at the top of a density-current head.

5.2 Thermodynamic structure of the line convection

We shall now consider the information shown by the shading in Figure 16(b) and also in Figure 16(c), which is a similar figure but for an RHI section (along a marginally different direction) 6 minutes later. The lighter shades represent radar reflectivity values in excess of 44dBz, the threshold being set high to exclude all of the precipitation echo except for that produced by the line convection itself. The peak values of 53 dBz observed over a horizontal scale of ½km correspond to rainfall intensities of roughly 100 mm h^{-1} sustained over ½ minute during the passage of the echo core. The darker shades represent areas with Linear Depolarization Ratios (LDRs) in excess of -24 dBz, and the purpose of depicting these is to draw attention to the height of the melting level which shows up as an LDR 'bright-band' between 2 and 3 km. In Figure 16(b) the melting level varies in height by less than 300 m but in Figure 16(c) there is a major variation of 900 m in the immediate vicinity of the line convection. A large proportion of the RHI cross-sections resembled Figure 16(c). As we now demonstrate, this anomalous behaviour of the melting level enables us to make interesting inferences about the thermodynamics of the line convection.

The LDR bright band can be taken as an indicator of the height of the zero-degree wet-bulb temperature. Knowing this height, it is possible to use a tephigram to estimate the θ_w characterising each part of the bright band. The values of θ_w at locations a, b and c in Figure 16(c) can be related to different parts of the flow field as follows: The lowest θ_w-value of 11.5°C is situated at location a (at a height of 2.2km) just behind the line convection within the head of the density current and is indicative of the cold air just behind the front. This is consistent with surface values plotted in Figure 14. The highest θ_w- value of 14.5°C, situated at location b where the bright band reaches a height of 2.9km, is within air that has ascended from the boundary layer ahead of the line convection (dashed streamline). Again, this is consistent with the observed surface values plotted in Figure 14.

At location c, the value of θ_w is 12.7°C; this location is also ahead of the line convection and it is situated at a height of 2.4km directly above the 14.5°C air that feeds the line convection. This implies a 1.8°C lapse in θ_w, ie significant low-level potential instability, in the inflow to the line convection. This supports the prediction of potential instability in the vicinity of the line convection, given by the mesoscale model (Figure 13(b)). (The corresponding θ_w-lapse from the model is actually 15 to 14°C). Potential instability may not have existed at all times and places along the line convection, however, because there were times (eg Figure 16(b)) when there was relatively little evidence of a bright-band undulation. Nevertheless, this emphasis on potential instability differs from that given by Browning and Pardoe (1973) who, whilst noting a small increase in θ_w very close to the surface, preferred to emphasise the near-neutral stability (ie nearly constant θ_w and air nearly saturated) in the lowest 2.5 km just ahead of line convection. The existence of potential instability in the inflow to CF II may be attributable to a vestigial dry intrusion associated with the remains

of CF I (just as the much better-defined dry intrusion associated with CF II was situated just in advance of CF III).

6. Performance of the mesoscale model

The purpose of this paper has been to use the model to the extent possible to assist in the understanding of the frontal structure and evolution, not to evaluate the model performance in detail. However, two contrasting aspects of its performance stand out and these will be mentioned briefly. The good aspect of the model is that it did reproduce the broad features, including the positions of the main fronts (Figure 11) and the overall pattern of precipitation (not shown). The bad aspect of the model is that it failed to reproduce either the intensity of the precipitation or the associated mesoscale and convective-scale circulations associated with CF II.

The nub of the problem appears to be the model's failure to reproduce the mesoscale transverse circulation accompanying CF II. Similar difficulties in reproducing the mesoscale transverse circulation responsible for a WCFR have also been encountered by Redelsperger and Lafore (1994) using a non-hydrostatic mesoscale model. The present shortcomings can be seen by comparing the observations in Figure 16(a) with the model-derived transverse circulation in Figure 13(d). The observed transverse circulation, expressed as velocities relative to the front, was manifested as a 10 to 12½ m s^{-1} rear-to-front wind component at levels from 1 to 1½ km and a front-to-rear wind component of -10 to -12½ m s^{-1} at 3 to 3½ km over almost the entire width of the mesoscale canopy of rearward-sloping ascent responsible for the WCFR. Although, as mentioned earlier, the model did produce a

rearward-sloping canopy with a dry finger beneath it (Figure 13(a)), it failed to produce any significant rear-to-front wind component in the region of the dry finger or indeed anywhere else near CF II. Moreover, the only significant front-to-rear components were in the boundary layer, and not in the rearward-sloping canopy as observed behind the line convection. This failure of the model to reproduce the mesoscale transverse circulation at CF II may have been linked to the additional failure to reproduce a sharp surface cold front. Even allowing for the limited model resolution (17 km grid), it produced nothing to indicate a strip of strong low-level convergence or vorticity that might be associated with the line convection and NCFR that was observed at 1800 UTC.

7. Synthesis and Conclusions

The archetypal mesoscale structure of an ana-cold front comprises a narrow cold-frontal rainband (NCFR) due to line convection embedded within a wide cold-frontal rainband (WCFR) due to slantwise ascent associated with a strong transverse-front mesoscale circulation (Browning 1990). Whereas most observational studies on the mesoscale have concentrated on this mature stage, this paper has explored by means of a case study how such a mature frontal system developed from pre-existing frontal features. The synoptic-scale context was one of frontal fracture accompanying rapid cyclogenesis (Shapiro and Keyser 1990). The cyclogenesis occurred on the cold side of the polar front ('instant occlusion' scenario as described by McGinnigle et al (1988)) during which multiple new cold fronts approached the frontolysing polar front. We have examined the mesoscale and convective structure and evolution of these fronts, concentrating especially on the way in which a new

(secondary) cold front merges with the frontolysing cold front. No generality is claimed for the particular evolution observed in this one case; rather, the aim of the investigation has been the more modest one of establishing the kinds of mesoscale substructure and interactions that may be important in this fairly common type of situation.

We have shown how one of the cold fronts (CF II) in this case study started as a shallow rope cloud, indicative of a sharp convergence line within the boundary layer, and then evolved over the period 00 to 18 UTC as summarized in Figure 17. At 0000 UTC in Figure 17, CF II was situated well over 100 km behind the main polar front, CF I. CF I was still active at 0000 UTC but by 0600 UTC it had largely frontolysed. As CF II approached the frontolysed cold front CF I at 1200 UTC, it was already producing a NCFR which soon developed into line convection. At this time CF II was not yet producing any obvious mesoscale (stratiform) cloud canopy of its own; however, it was surrounded by scattered outbreaks of rain related to the deepening of *rearward*-trailing cloud plumes associated with the reinvigorating CF I. Each of these plumes could be attributed to the renewed ascent of trackable patches of moist air created 18 hours earlier by vigorous convective storm cells, with *forward*-trailing anvils, along the original polar front (CF I) before it began to frontolyse. The change in the orientation of the CF I anvil plumes is indicative of a change from a kata- to a locally ana-frontal (direct) circulation. Over the period from just before 1200 to 1500 UTC, the development of this ana-circulation led to a broad and quite intense WCFR within which the CF II NCFR could be glimpsed in places. Then during the next 3 hours the CF II line convection itself intensified and it began to produce a stratiform cloud canopy of its own at mid-levels beneath the CF I plumes. By 1800 UTC the rearward-ascending outflow

due to CF II had taken over as the major contributor to the ana-circulation and the predominant producer of precipitation in the WCFR.

Some aspects of the broad-scale thermodynamic structure and precipitation pattern were reasonably well represented by the Met Office operational mesoscale model. One feature that was represented was the penetration of the finger of 'dry-intrusion' air with low θ_w just behind the front CF II where it became sharp at low levels. However, the low-θ_w air in the model did not have the observed strong rear-to-front component of relative flow (>10 m s^{-1}) towards the front and it failed to create the observed density current-like nature of the surface front. The model also failed to generate the observed mesoscale canopy of strong front-to-rear relative flow (>10 m s^{-1}) that was fed by the outflow from the line convection. The large overall transverse circulation which the model failed to reproduce is evidently the key to the cold frontal structure. It led to the development of a WCFR due to the creation of a combined rearward-ascending outflow from CF II and from the reinvigorated CF I.

The observations indicate that the rear-to-front wind component associated with the finger of low-θ_w dry-intrusion air behind CF II led to a density current-like feature that forced the warm boundary-layer air ahead of it to ascend in an organized way into the canopy of rearward-sloping mesoscale ascent. There may have been a positive feedback process in which the cooling due to evaporation and melting of precipitation falling from the canopy into the dry finger (Clough and Franks 1991, Yang and Houze 1995) led to an intensification of the mesoscale circulation which in turn led to a tendency for sharpening of the surface front. However, the front had produced a rope cloud indicative of a sharp surface convergence line even before the generation of extensive precipitation. Indeed this went on to develop into a

NCFR, with evidence of 2-d line convection, again,just before the development of the WCFR associated with the mesoscale transverse circulation. This, together with the fact that the rear-to-front inflow was strongest at the trailing edge of the WCFR, suggests that the precipitation processes probably were not the primary factor in the development and that there may have been a mesoscale transverse circulation already in association with the dry intrusion when it first entered the region of cyclogenesis. An example of a mesoscale circulation in the dry air which was associated with a shallow rope-like cloud is given in Browning (1995). Unfortunately we do not yet have a proper understanding of the dynamics of such events.

The nature of the cold fronts upstream of the developing low centre in this study may be summarised as follows:

- Multiple cold fronts occurred within the dry-intrusion region prior to cyclogenesis.
- The early-stage cold fronts, with the exception of the initial one, were all observed as thin lines of, often rope-like, boundary-layer clouds beneath the advancing dry intrusion.
- Prior to cyclogenesis the first cold front was producing a major polar-front cloud band, with embedded thunderstorms, but it underwent frontolysis prior to cyclogenesis as the dry-intrusion air overran it (kata-cold front structure).
- As cyclogenesis got underway the kata-cold frontal circulation was replaced by an ana-cold frontal circulation: this could be ascertained from the switch from forward-trailing to rearward-trailing convectively-generated cloud plumes associated with the first cold front.

- Only two of the many cold fronts persisted as surface features during cyclogenesis. At the onset of the ana-circulation one of these developed intense line convection and a rearward-sloping stratiform canopy due to the strong transverse circulation.
- The strong transverse circulation associated with the dominant cold front appeared to be forced rather more by the large-scale dynamics than by precipitation-related mesoscale processes, although the relative importance of these processes probably varies from case to case.

Acknowledgement

We are grateful to John Goddard for provision of data from the Chilbolton radar and to Danny Chapman for producing the cross-sections from it.

References

AMS 1996 Proceedings of the seventh conference on mesoscale processes. Reading, Sept 1996. Amer.Meteorol.Soc., Boston, Mass.

Bader, M.J., Forbes, G.S., Grant, J.R., Lilley, R.B.E. and Waters, A.J. 1995 Images in weather forecasting, Cambridge Univ. Press, 499 pp.

Browning, K.A., 1990 Organization of clouds and precipitation in extratropical cyclones Pp 129-153 in *Extratropical cyclones* Eds C.W. Newton and E.O.Holopainen. Am.Meteorol.Soc., Boston, Mass.

Browning, K.A. 1995 On the nature of the mesoscale circulations at a kata-cold front, *Tellus*, **47A**, 911-919.

Browning, K.A., 1996 Mesoscale aspects of extratropical cyclones: an observational perspective. To be published in Bergen post-conference book Ed. M. Shapiro, Am. Meteorol. Soc., Boston, Mass.

Browning, K.A., Ballard, S.P. and Davitt, C.S.A. 1996 High-resolution analysis of frontal fracture, *Mon.Wea.Rev.*, (Submitted).

Browning, K.A., Clough, S.A., Davitt, C.S.A., Roberts,N.M., Hewson, T.D. and Healey, P.G.W. 1995 Observations of the mesoscale sub-structure in the cold air of a developing frontal cyclone, *Q.J.R.Meteorol.Soc.*, **121**, 1229-1254.

Browning, K.A., and Pardoe,C.W. 1973 Structure of low-level jet streams ahead of mid-latitude cold fronts, *Q.J.R.Meteorol.Soc.*, **99**, 619-638

Browning, K.A. and Roberts, N.M. 1994 Structure of a frontal cyclone, *Q.J.R.Meteorol.Soc.*, **120**, 1535-1557.

Carbone, R.E., 1982 A severe frontal rainband. Part 1: Stormwide hydrodynamic structure. *J.Atmos.Sci.*, **39**, 258-279.

Clough, S.A., and Franks, R.A.A. 1991 The evaporation of frontal and other stratiform precipitation, *Q.J.R.Meteorol.Soc.*, **117**, 1057-1080.

Hobbs, P.V., and Persson, P.O.G. 1982 The mesoscale and microscale structure of clouds and precipitation in midlatitude cyclones, V: The substructure of narrow cold frontal rainbands. *J.Atmos.Sci.*, **39**, 280-295.

Houze, R.A., Hobbs, P.V., Biswas, K.R. and Davis, W.M. 1976 Mesoscale rainbands in extratropical cyclones, *Mon.Wea.Rev.*, **104**, 868-878.

Kreitzberg, C.W. and Brown, H.A. 1970 Mesoscale weather systems within an occlusion, *J.Appl.Meteorol.*, **9**, 417-432.

McGinnigle, J.B., Young, M.V. and Bader, M.J. 1988 The development of instant occlusions in the North Atlantic, *Meteorol.Mag.*, **117**, 325-341.

Parsons, D.B. 1992 An explanation for intense frontal updrafts and narrow cold-frontal rainbands, *J.Atmos.Sci.*, **49**, 1810-1825.

Redelsperger, J-L. and Lafore, J-P. 1994 Non-hydrostatic simulations of a cold front observed during the Fronts 87 experiment, *Q.J.R.Meteorol.Soc.*, **120**, 519-555.

Saarikivi, P. and Puhakka, T. 1990 The structure and evolution of a wintertime occluded front. *Tellus*, **47A**, 122-139.

Scorer, R.S. 1986 Cloud investigation by satellite, Ellis Horwood (Chichester). pp vi + 314

Shapiro, M.A., Hampel, T., Rotzoll, D. and Mosher, F. 1985 The frontal hydraulic head: a micro-α scale (~ 1 km) triggering mechanism for mesoconvective weather systems. *Mon.Wea.Rev.*, **113**, 1166-1183.

Shapiro, M.A. and Keyser, D. 1990 Fronts, jet streams and the tropopause. Pp 167-191 in *Extratropical cyclones* Eds. C.W.Newton and E.O.Holopainen. Amer.Meteorol.Soc., Boston, Mass.

Smith, R.K., Reeder, M.J., Tapper, N.J. and Christie, D.R. 1995 Central Australian cold fronts, *Mon.Wea.Rev.*, **123**, 16-38.

Smull, B.F. and Houze, R.A., Jr. 1987 Rear inflow in squall lines with trailing stratiform precipitation. *Mon.Wea.Rev.*, **115**, 2869-2889.

Yang, M-J and Houze, R.A., Jr. 1995 Sensitivity of squall-line rear inflow to ice microphysics and environmental humidity. *Mon.Wea.Rev.*, **123**, 3175-3193.

Zillman, J.W. and Price, P.G. 1972 On the thermal structure of mature Southern Ocean cyclones. *Austral.Meteorol.Mag.*, **20**, 34-48.

Figure Legends

Figure 1 Structure of a developing extratropical cyclone (from Browning 1996). The cyclone centre (L) is travelling towards the top right. The surface warm front is shown conventionally. Part of the bent-back front (cd) is plotted as a cold front with closely-spaced frontal symbols. The main surface cold front (ab) is shown similarly. In between the two sharp surface cold fronts (bc) there is a diffuse surface cold front drawn dashed with widely-spaced frontal symbols. The cold front drawn with open symbols (bd) is an upper cold θ_w-front (UCF) marking the leading edge of the dry intrusion. Principal airflows, drawn relative to the system, are: the main warm conveyor belt (W1) (solid lines), the secondary warm conveyor belt (W2) (long-dash lines), the cold conveyor belt (CCB) (short-dash lines) and the dry intrusion (dotted lines). The cold-air sides of the main cloud features are drawn scalloped: the polar-front cloud band is due to W1, and the cloud head is due to the combined effect of W2 and the CCB. Precipitation reaches the surface along the left side of W1, near the cold fronts, and above the warm frontal zone; precipitation also falls from the inner parts of the cloud head starting at the bent-back front. The two main areas of precipitation are separated by a dry slot where the shallow W2 flow is capped by the dry intrusion. The dry slot is usually characterized by partial shallow cloudiness.

Figure 2 Synoptic overview of the case studied in this paper, from a combination of Meteosat infra-red imagery and output from the operational Met Office Limited Area Model at (a) 06, (b) 12, (c) 18 UTC,
24 October and (d) 00 UTC 25 October 1995. Lines are msl isobars at 4 mb intervals. Cloud areas II and III are marked in (a); these merged into a single cloud head just southwest of the low centre L by 12 UTC (b). Each of the cloud areas was associated with its own shallow cloud line extending to the south of it (more clearly evident in Figs. 3 and 4). The grey scale is linear between -54°C (palest grey) and +16°C (darkest grey).

Figure 3 Analysis for 15 UTC, 24 October 1995 showing multiple cold fronts (thin lines) and msl pressure (at 4 mb intervals). The main cold fronts are labelled I, II, III and IV. Front I is the original polar front which by this time had frontolysed. The two fronts shown between I and II were short-lived features. Meteosat infra-red imagery is shown as a background; the grey scale is linear between -48°C (palest grey) and +12°C (darkest grey).

Figure 4 (a) Visible and (b) infrared Meteosat images at 1100 UTC, 24 October 1995, showing cloud lines associated with Cold Fronts I, II and III trailing southwards from cloud heads over and to the southwest of Ireland. The grey scale is linear between -35°C (palest grey) and +15°C (darkest grey). Circles show coverage of the Cornwall radar.

Figure 5 Hourly positions of Cold Front II deduced from Meteosat and radar imagery from 07 to 20 UTC, 24 October 1995. Bold portions of the lines indicate regions of line convection inferred by radar. Successive frontal positions are

given additional constant displacement to the right in order to provide space to show cloud plumes extending rearwards from the northern end of the line - see darkly shaded areas from 07 to 13 UTC (the entire cloud head area associated with CF II being shown for 09 UTC only). Arrows show the displacement of specific cloud elements. The lightly shaded region bounded by dashed lines denotes the western edge of an area of higher cloud due to CF I which increasingly obliterated cloud due to CF II after 13 UTC. The inset shows frontal positions without additional displacements in order to clarify the movement of CF II in an earth-relative frame of reference. Also shown in the inset are pressure kicks (plotted in mb within the small circles) for 6 stations during the passage of CF II. The large circle in the inset shows the coverage of the Cornwall radar.

Figure 6 Radar displays (a, b and c) and corresponding Meteosat infrared images (d, e and f) at 12 UTC (a and d), 13 UTC (b and e) and 14 UTC (c and f) on 24 October 1995. Coverage of the Cornwall radar is shown by the large circles with radius 210 km. The four grey shades in (a), (b) and (c) represent rainfall intensities <2, 2-4, 4-8 and >8mm h^{-1}. The grey shades in (d), (e) and (f) represent cloud-top temperature according to a linear scale between -28°C (palest grey) and +8°C (darkest grey). The position of CF II is indicated in (a), (b) and (c). Areas of upper cloud associated with CF I that developed into major plumes which overran CF II are identified by small circles labelled A, B, C and D.

Figure 7 Radar network picture for 18 UTC, 24 October 1995. The four grey shades represent rainfall intensities of <2, 2-4, 4-8 and >8 mm h^{-1}. The main belt of rain extending from France to Scotland is due to CFII, with a small contribution from CF I. The thin line of rain extending from southwest England southwards near 5°W to Brest, with a more general area of rain over extreme southwest England, is associated with CF III. The rain area over Ireland is associated with the main cloud head associated with CF II and CF III. A coloured version of the 1830 UTC picture is shown on the cover of AMS (1996).

Figure 8 Meteosat infrared images and corresponding radar network pictures for 16 UTC (a and b) and 17 UTC, 24 October 1995 (c and d). The grey shades in (a) and (c) show cloud-top temperature according to a linear scale between -45°C (palest grey) and 0°C (darkest grey). Cloud plumes associated with CF I are labelled A, B, C, D & E. The five grey shades in (b) and (c) show rainfall intensities <2, 2-4,4-8, 8-16 and >16 mm h^{-1}.

Figure 9 Successive 2-hourly positions on 24 October 1995 of cloud plume C associated with Cold Front I, anchored with respect to the infrared imagery at the beginning (01 UTC) and end (17 UTC) of the tracks. Other cloud plumes (eg D and E) could be followed along almost parallel tracks. CF I is shown by the dashed lines through the upwind ends of the plumes at 01 and 17 UTC. The grey shades represent cloud-top temperatures according to a linear scale between -45°C (palest grey) and +9°C (darkest grey). The 01 and 17 UTC

images show the cloud plumes to be forward-trailing and rearward-trailing, respectively, and a cloud outline and arrow is marked in each case to emphasize this.

Figure 10 Successive hourly positions of Cold Front III, inferred from satellite and radar imagery, from 13 to 21 UTC, 24 October 1995. The inset shows CF III at the time (17 UTC) of maximum wave amplitude, in relation to the cloud plumes associated with CF III and CF II.

Figure 11 Output from the mesoscale model for 18 UTC, 24 October 1995, showing wet-bulb potential temperature, θ_w (a and b) and relative humidity (c and d) at 850 mb (a and c) and 650 mb (b and d). Contours of θ_w are plotted at 0.5°C intervals. Relative humidity is plotted at intervals of 5% (shaded in excess of 90%). Frontal analyses are consistent with observational evidence: radar line convection for the surface cold fronts and a line of radar-observed convective cells for the upper cold front. The two arrows denote axes of two fingers of dry-intrusion air referred to in the text.

Figure 12 Plan sections at 850mb (a, b and c) and cross-section (d) showing relative humidity (at 5% intervals, shaded >90%) as derived from the 12 UTC forecast run of the mesoscale model on 24 October 1995. (a): 12 UTC, (b): 15 UTC, (c) and (d): 18 UTC. Positions of Cold Front II where it is a sharp feature, as inferred from radar, are plotted in (a), (b) & (c). The section in (d) is orientated along the axis of the dry intrusion (XX in (c)).

Figure 13 Cross- sections at right angles to Cold Front II (along AB in Figure 11(c)) showing (a) relative humidity (contours at 5% intervals, shaded >95%), (b) wet-bulb potential temperature (contours every 0.5°C), (c) front-parallel wind component (contours every 5 m s^{-1}) and (d) front-normal wind component (contours every 2 m s^{-1}), as derived from the mesoscale model at 18 UTC, 24 October 1995. The vertical arrow extending up to almost 700 mb represents the line convection at Cold Front II. The dashed frame within Figure 13(d) shows the region covered by the Doppler radar cross-section in Figure 16(a).

Figure 14 Detailed surface and frontal analysis for 18 UTC, 24 October 1995. Thin solid lines are isobars at 2 mb intervals. Dotted lines show wet-bulb potential temperature at 2°C intervals: individual station values are also plotted (a dot means ½). Areas warmer than 12 and 14°C, respectively, are shaded lightly and moderately, and the axes of the main warm-conveyor-belt flows are represented by bold arrows. Also shown are Cold Fronts II and III and the bent-back front; portions of surface cold fronts with and without line convection, respectively, are marked with and without solid frontal symbols, and the upper cold θ_w-frontal part of CF II is marked with open frontal symbols.

Figure 15 Tracings of autographic charts showing (a) msl pressure and (b) wind direction during the passage of Cold Front II at approximately 18 UTC at Middle Wallop, 51° 19'N, 01° 34'W (Station M), Shawbury, 52° 48'N, 02° 40'W

(Station S) and Ronaldsway, 54° 05'N, 04° 38'W (Station R); the traces have been displaced so that T=O corresponds to the passage of CF II. The locations of Stations M, S and R correspond respectively to the plotted values 2, 2 and 0 near the 18 UTC position of the front in the inset to Figure 5.

Figure 16 Cross-sections from the Chilbolton multiparameter Doppler radar at right angles to Cold Front II at 1839 UTC (a and b) and 1845 UTC (c) on 24 October 1995. West is to the left and the front is travelling from left to right. Shading in (a) shows the transverse wind component relative to the front according to the scale at the foot of the figure. The speckled region at the top of the diagram corresponds to radar noise where the signal is weak. A coloured version is shown on the cover of AMS (1996). Solid curves in (a) are streamlines derived using a 2-d assumption. Solid curves in (b) and (c) are also streamlines but for an enlarged portion of the front near the line convection. Flux between adjacent streamlines in (a) and (b), respectively, is 5 and 1 kg s^{-1} per kilometre perpendicular to the diagrams. The pale shading in (b) and (c) shows radar reflectivity in the range 44 to 53 dBz. The darker shading represents the melting layer as inferred from values of linear depolarization ratio greater than -24dB. The locations a, b and c in (c) are discussed in the text.

Figure 17 Schematic representation of the evolution of cloud and precipitation associated with Cold Fronts I and II during the period of cyclogenesis. Left side: cross-sections. Right side: plan views. Cloud is stippled and precipitation hatched. Open arrows denote dry intrusions: other arrows (1800 UTC only) represent saturated mesoscale ascent.

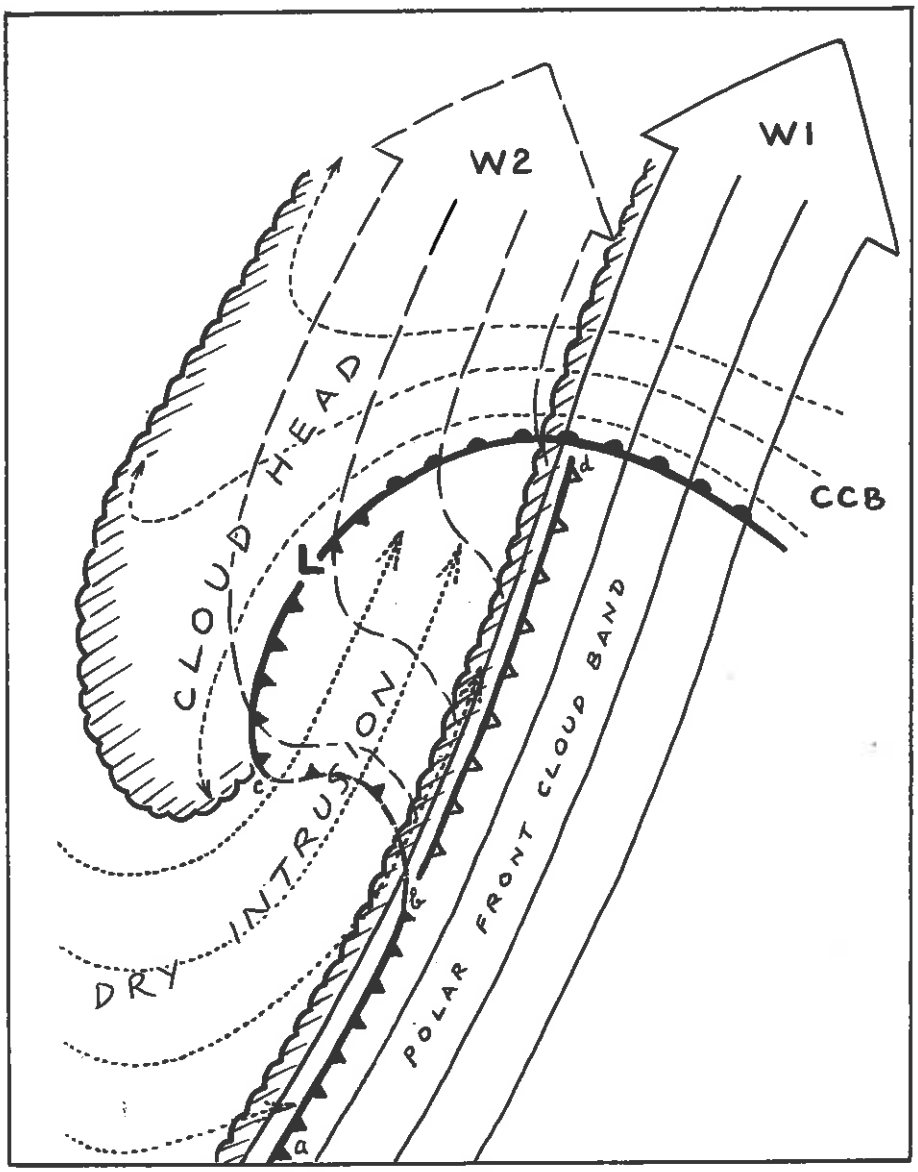
W2
W1
CLOUD HEAD
CCB
DRY INTRUSION
POLAR FRONT CLOUD BAND
L
a
c
d

Fig 1

Figure 2

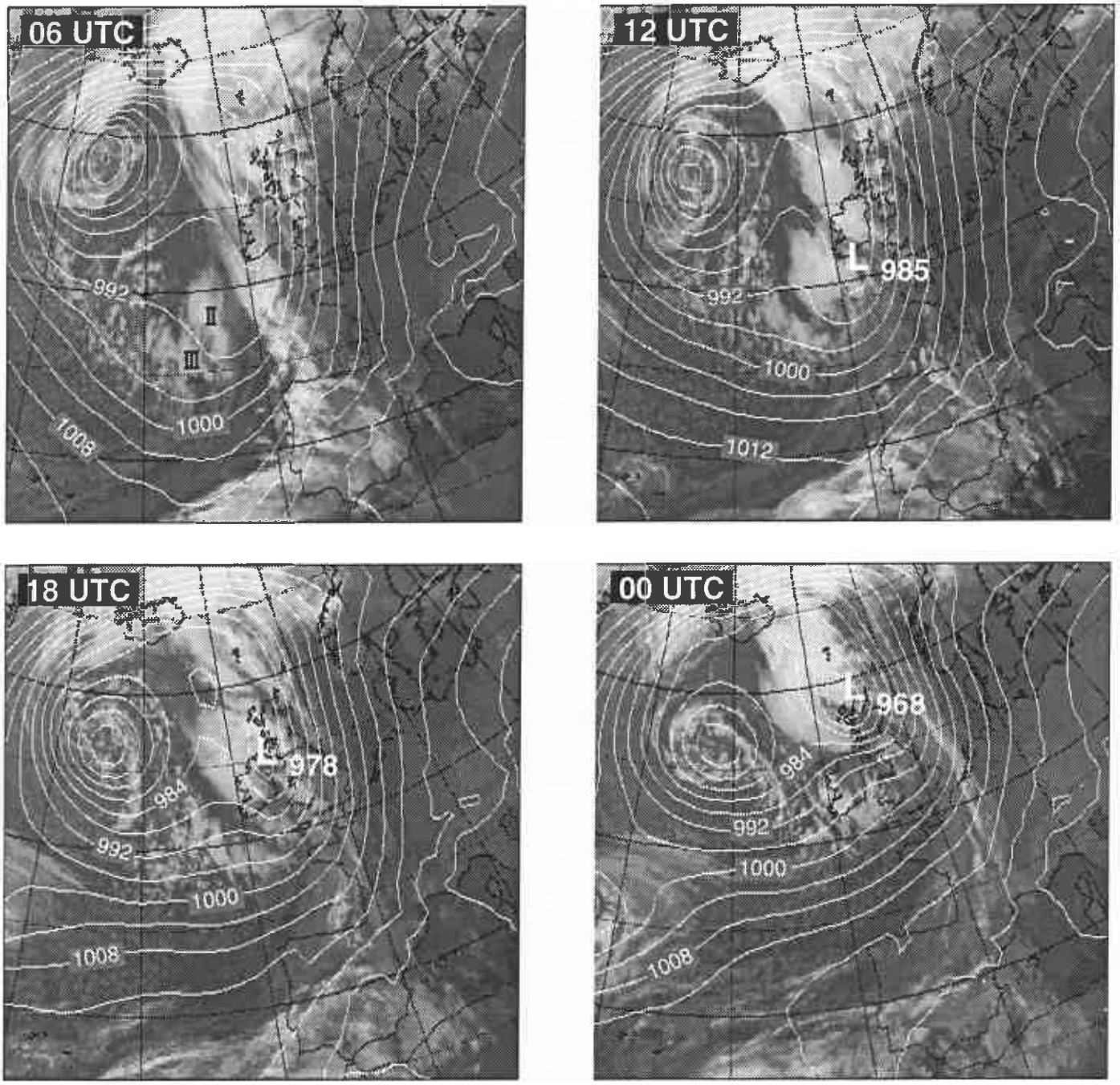
06 UTC
992
II
III
1000
1008
12 UTC
L 985
992
1000
1012
18 UTC
L 978
984
992
1000
1008
00 UTC
L 968
984
992
1000
1008

Figure 3

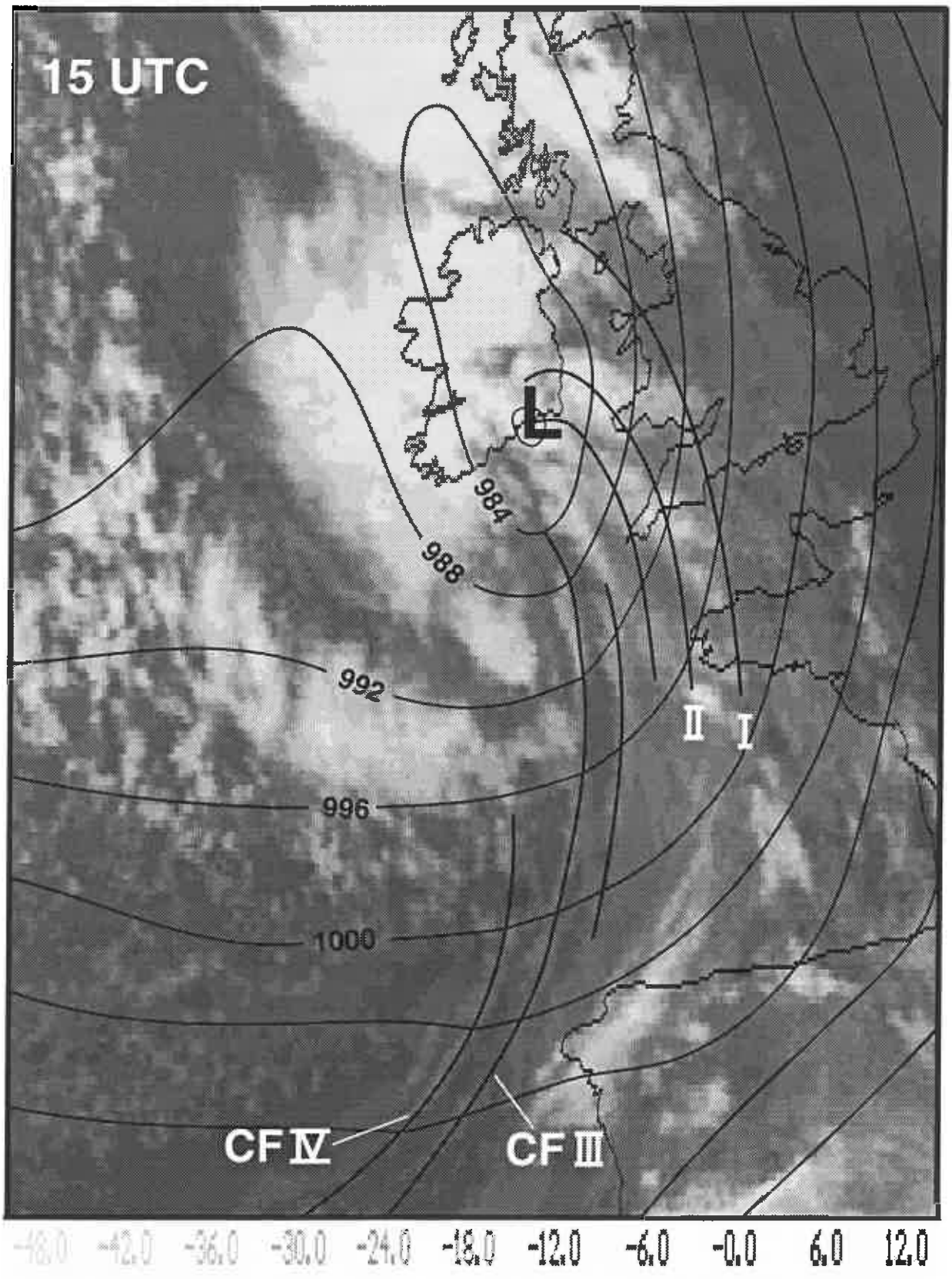
15 UTC
L
984
988
992
996
1000
II
I
CF IV
CF III
-48.0
-42.0
-36.0
-30.0
-24.0
-18.0
-12.0
-6.0
-0.0
6.0
12.0

Figure 4

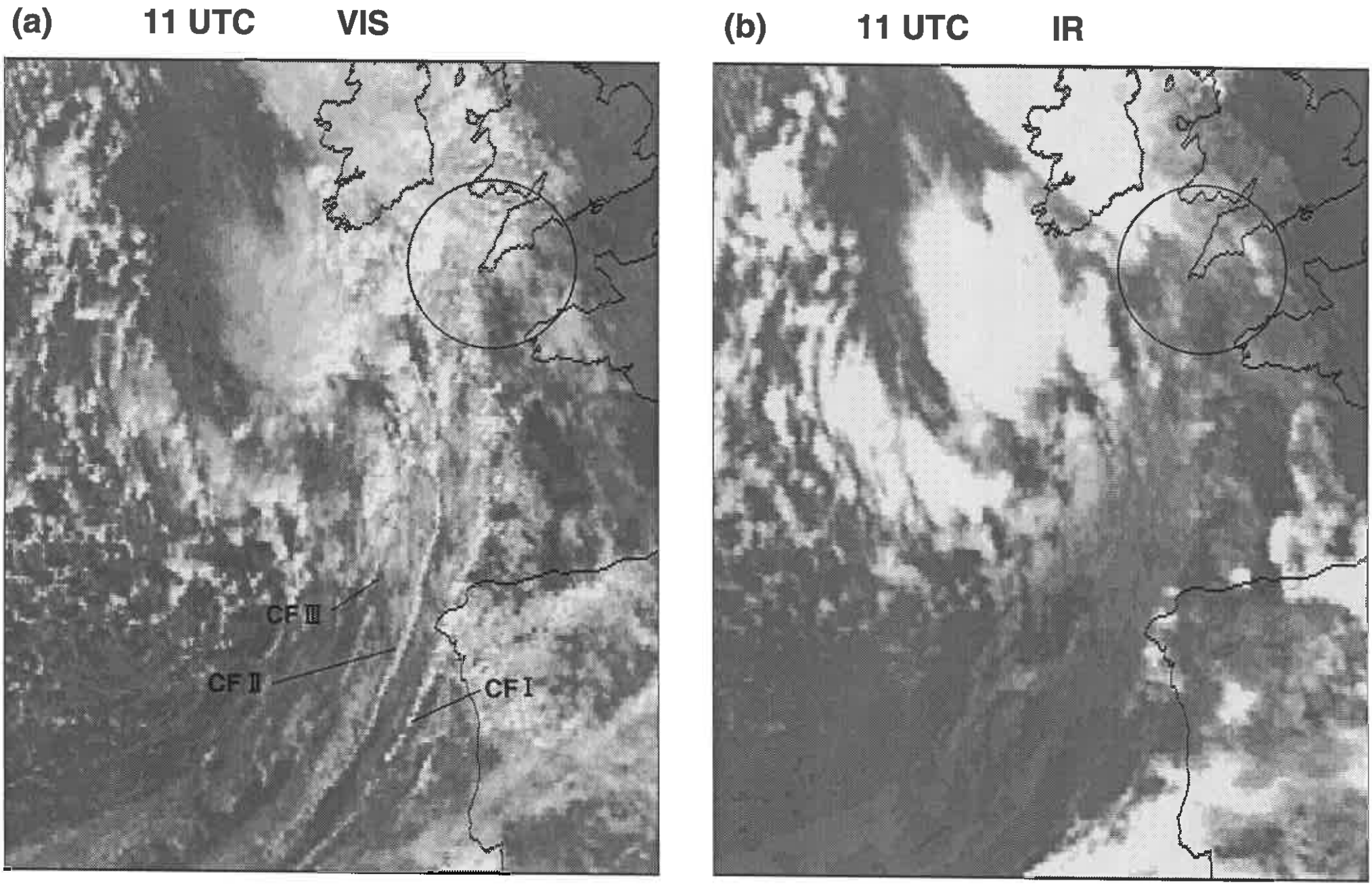

Figure 5

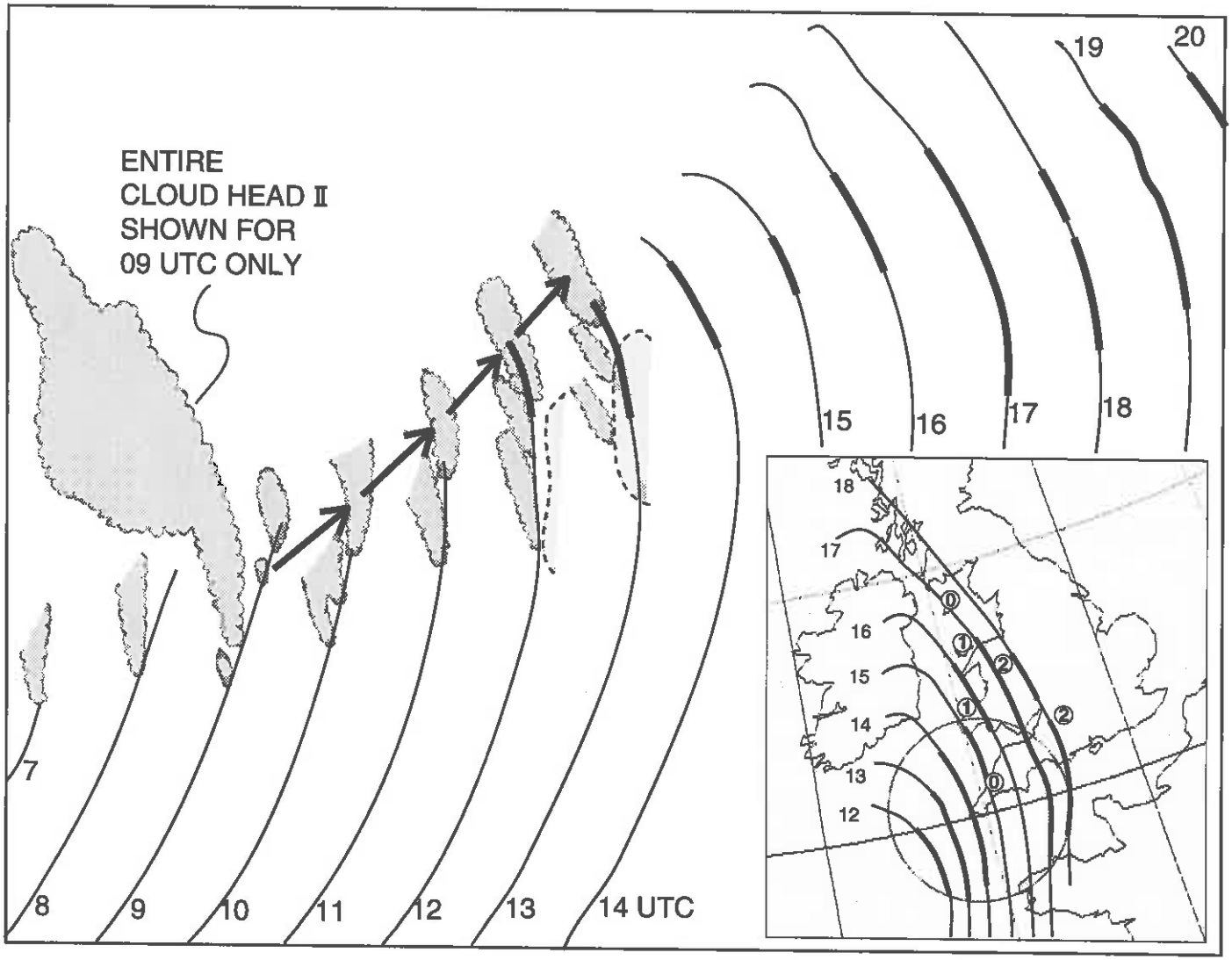
ENTIRE
CLOUD HEAD II
SHOWN FOR
09 UTC ONLY
7
8
9
10
11
12
13
14 UTC
15
16
17
18
19
20
18
17
16
15
14
13
12
0
1
2
1
2
0

Figure 6

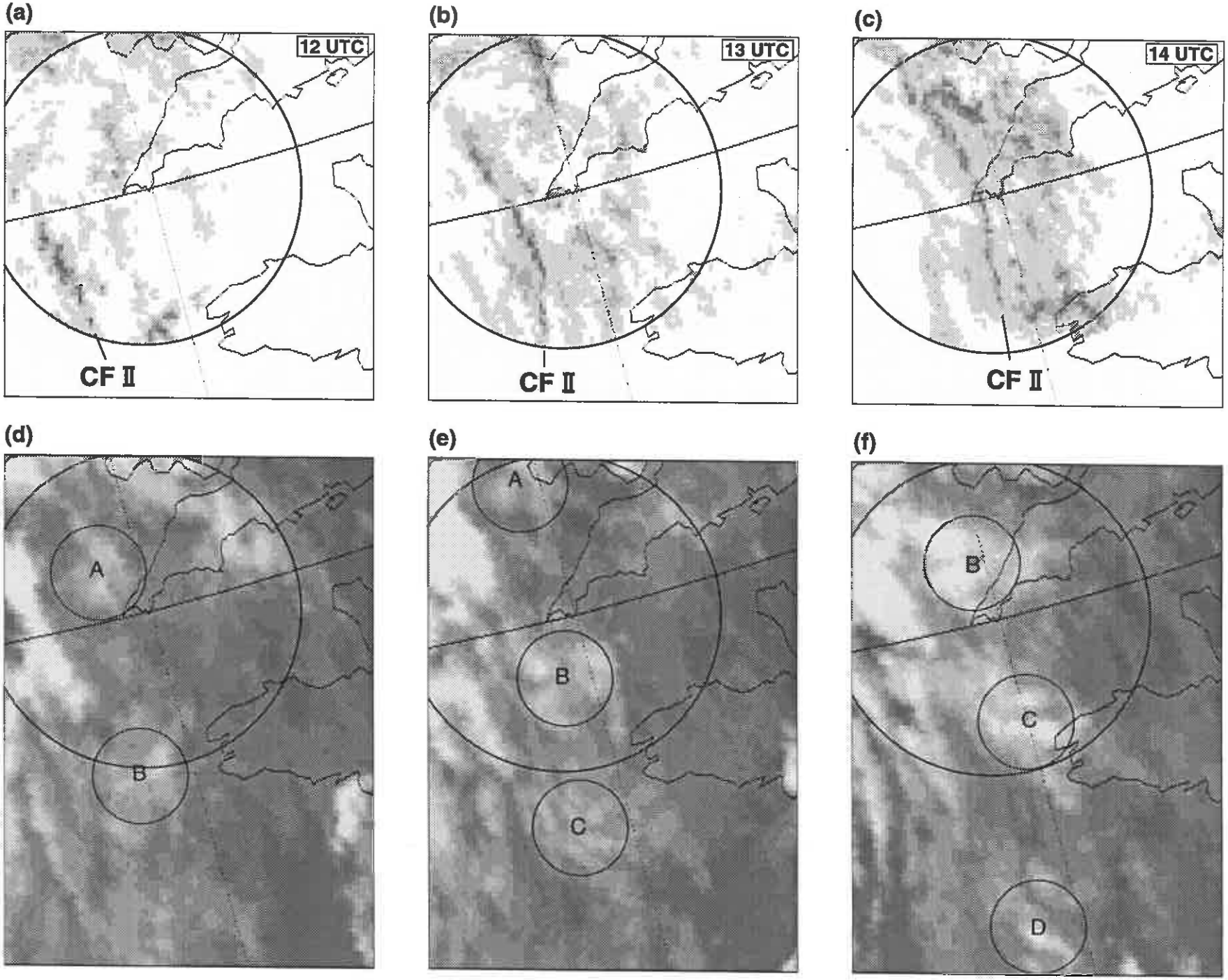

Figure 7

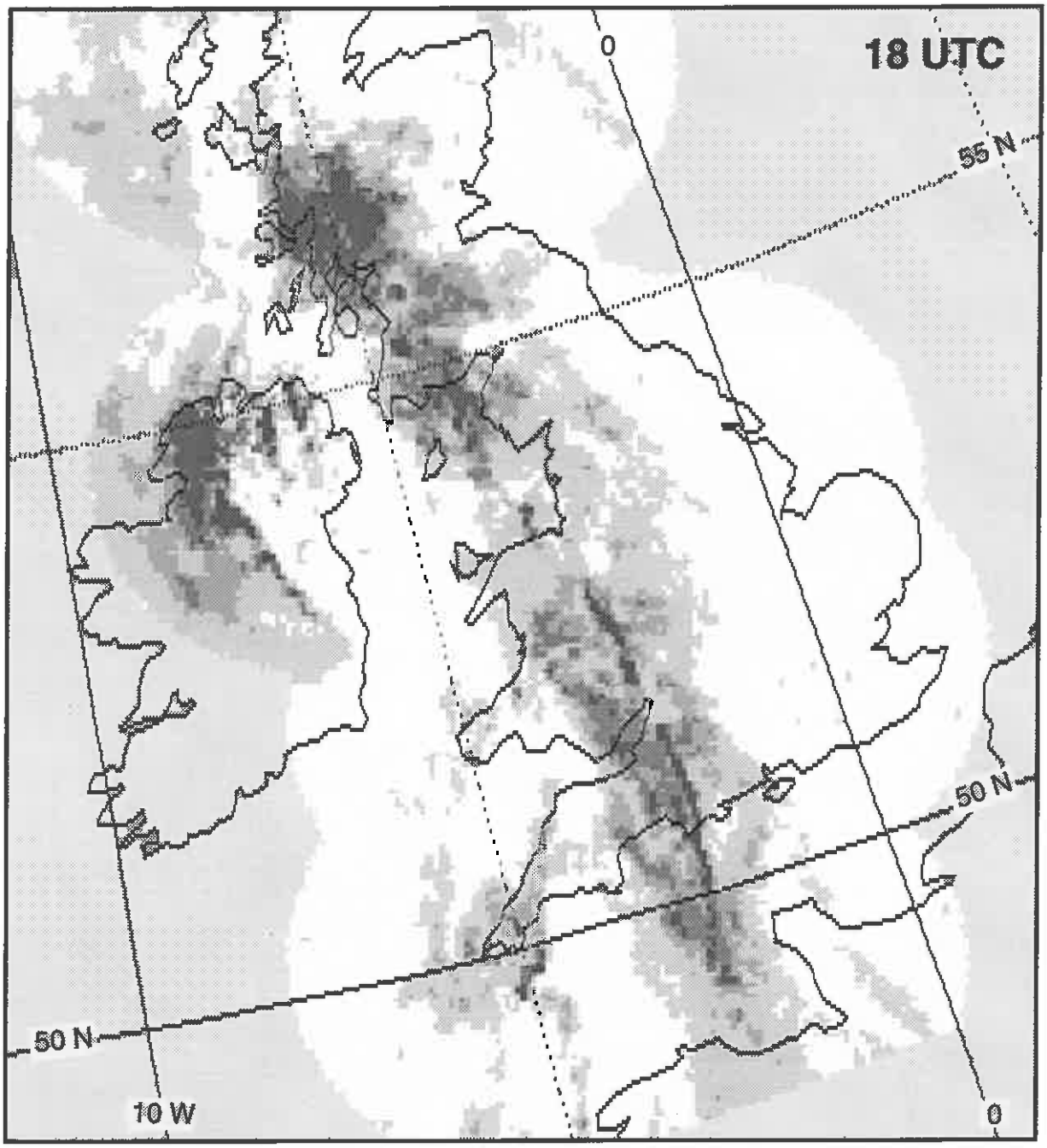

Figure 8

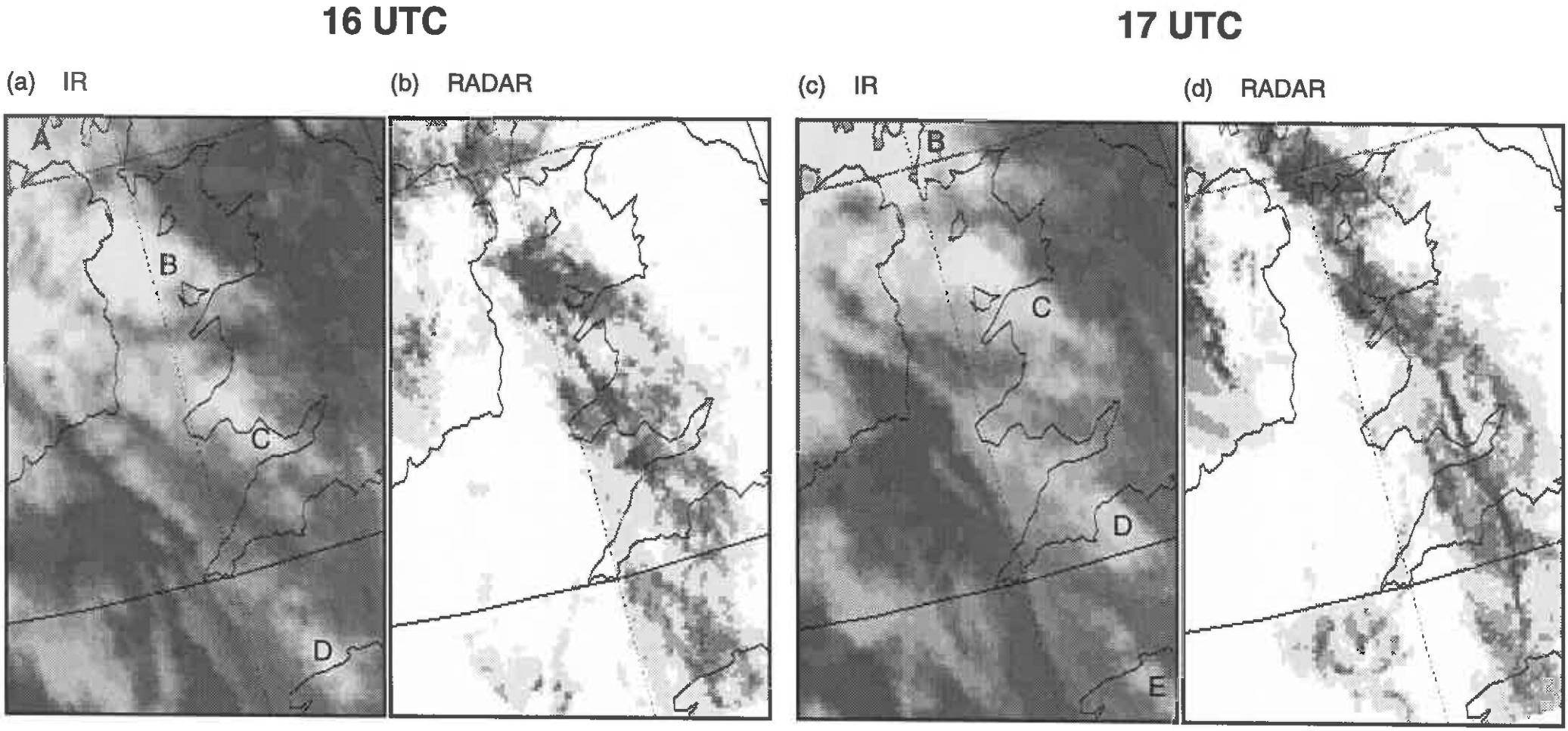

Figure 9

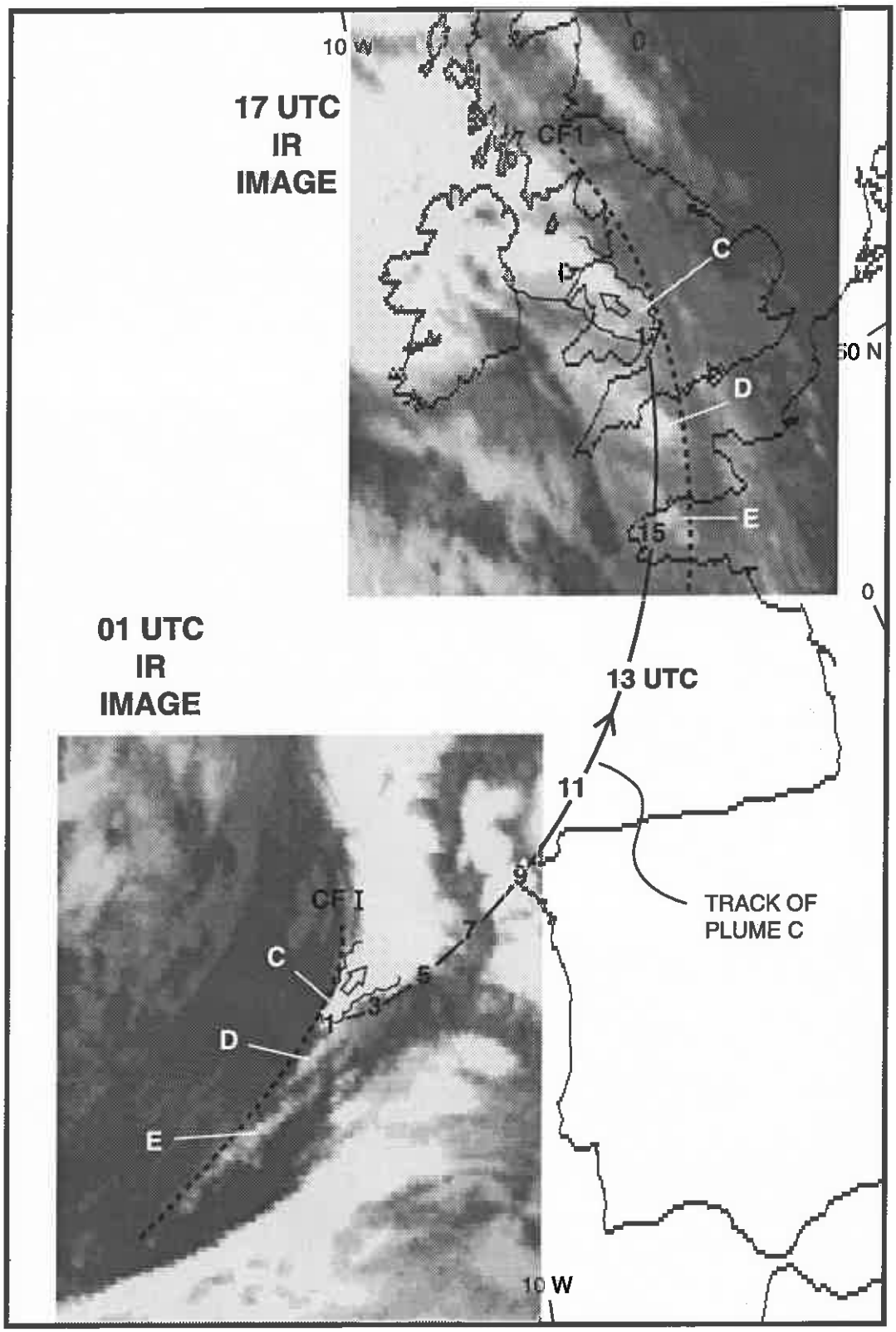
10 W
17 UTC
IR
IMAGE
CF1
C
D
E
15
13 UTC
11
9
7
5
3
1
0
50 N
01 UTC
IR
IMAGE
CF I
C
D
E
TRACK OF
PLUME C
10 W

Figure 10

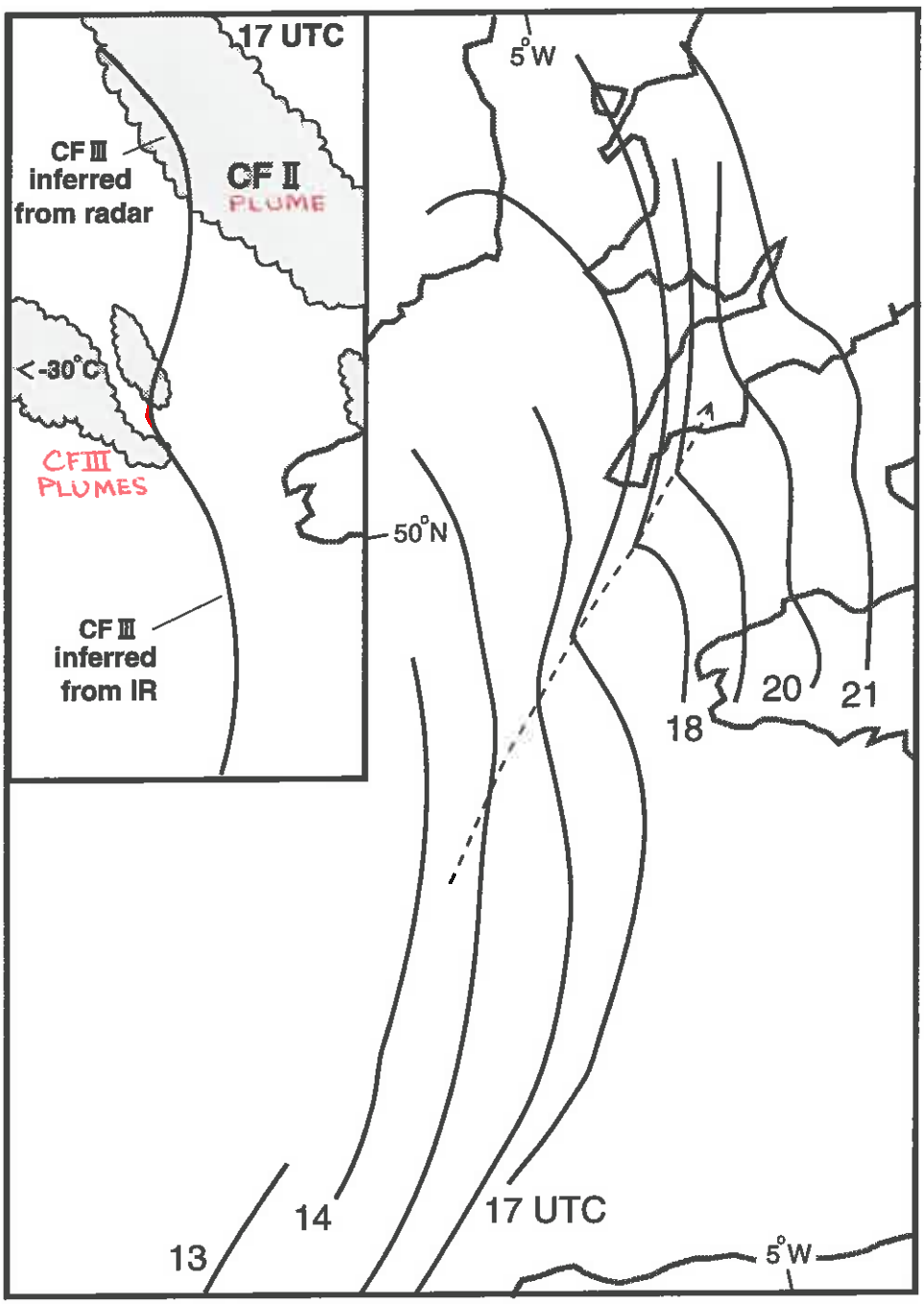
17 UTC
CF III
inferred
from radar
CF II
PLUME
< -30°C
CFIII
PLUMES
CF III
inferred
from IR
5°W
50°N
18
20
21
13
14
17 UTC
5°W

THETAW 850mb
VALID AT 18Z ON 24/10/1995 DAY 297 DATA TIME 18Z ON 24/10/1995

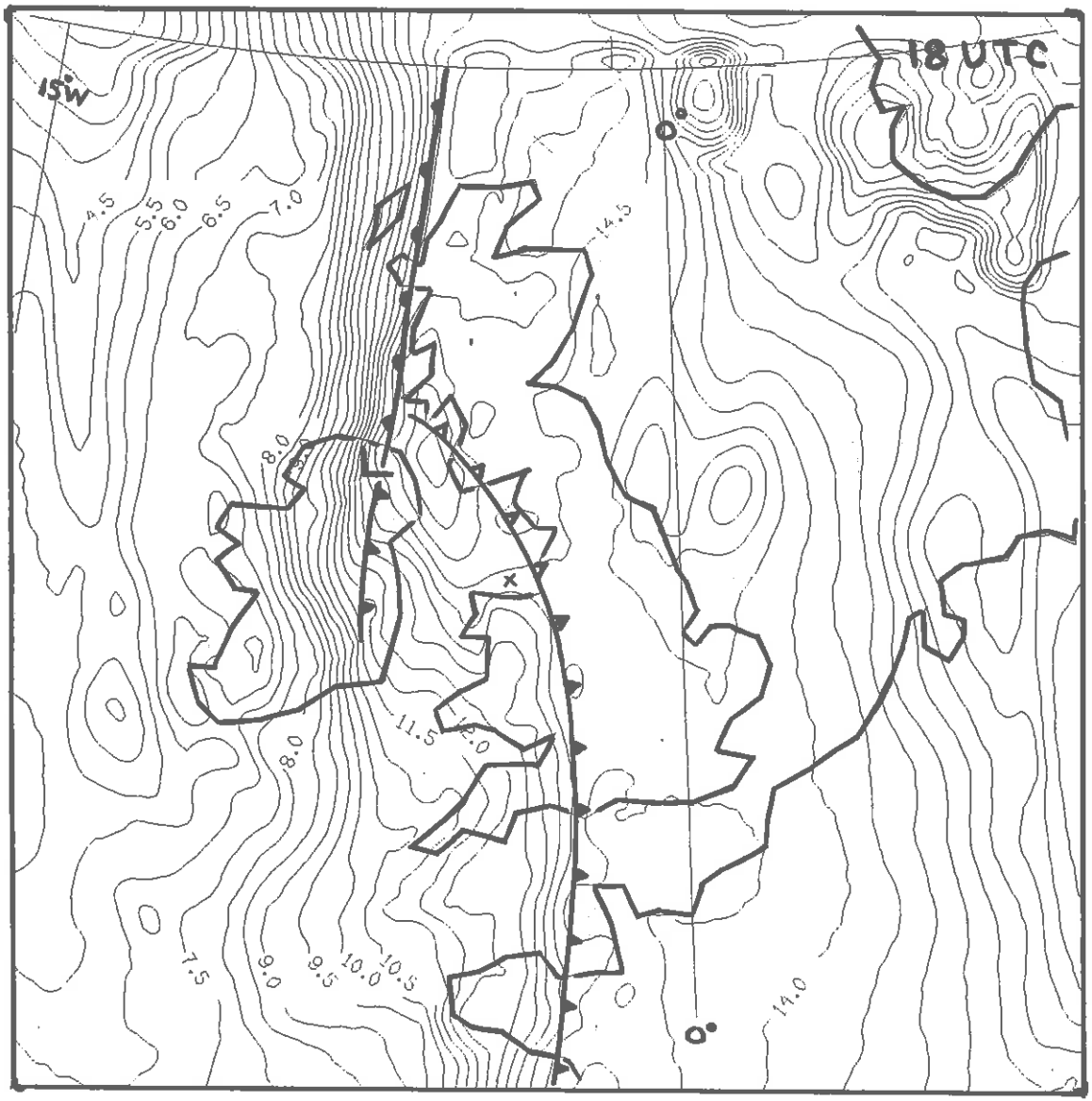

(a)

Fig 11 (a)

THETAW 650mb
VALID AT 18Z ON 24/10/1995 DAY 297 DATA TIME 18Z ON 24/10/1995

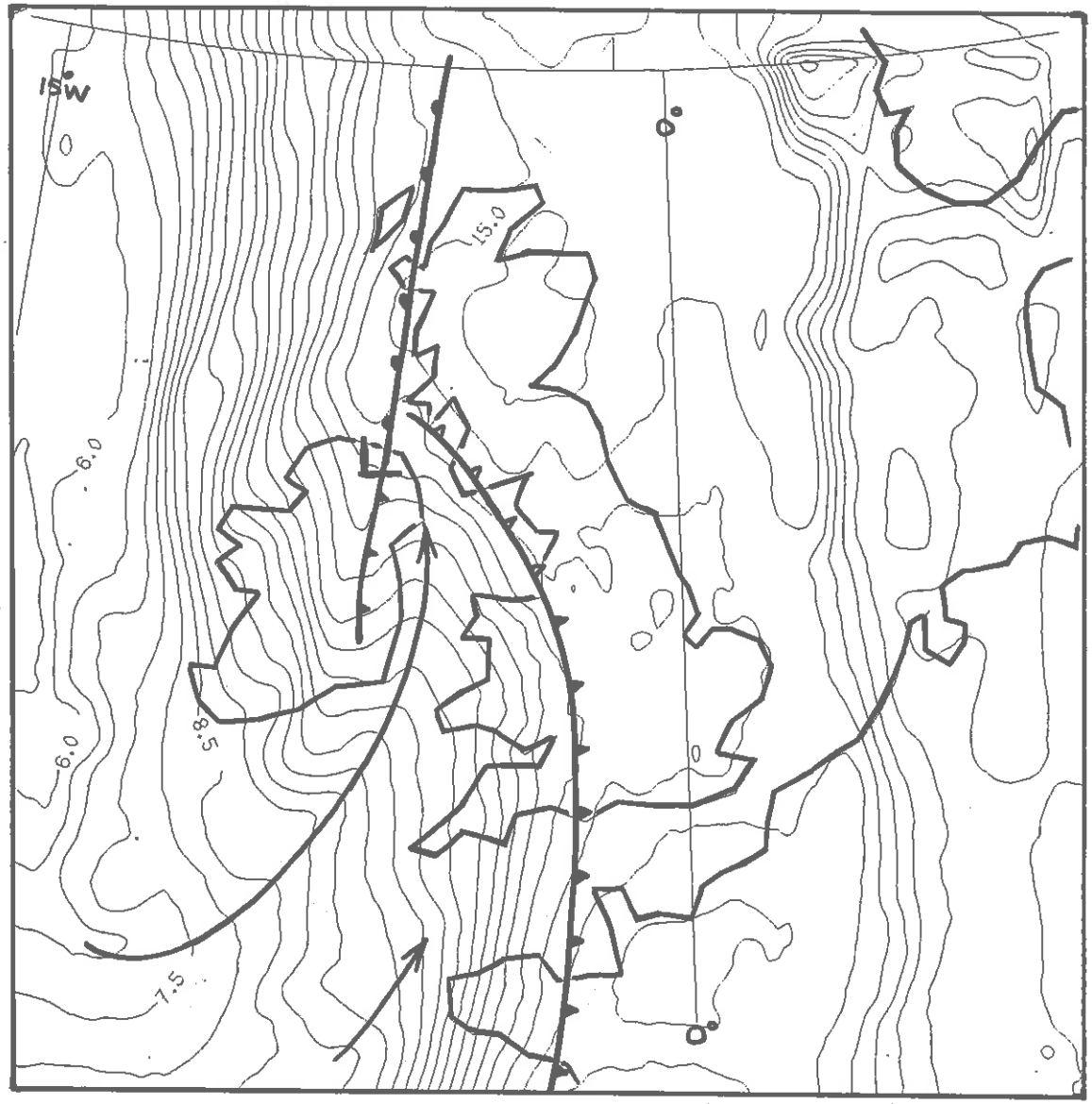

(b)

Fig 11 (b)

RELATIVE HUMIDITY 850mb
VALID AT 18Z ON 24/10/1995 DAY 297 DATA TIME 18Z ON 24/10/1995

(c)

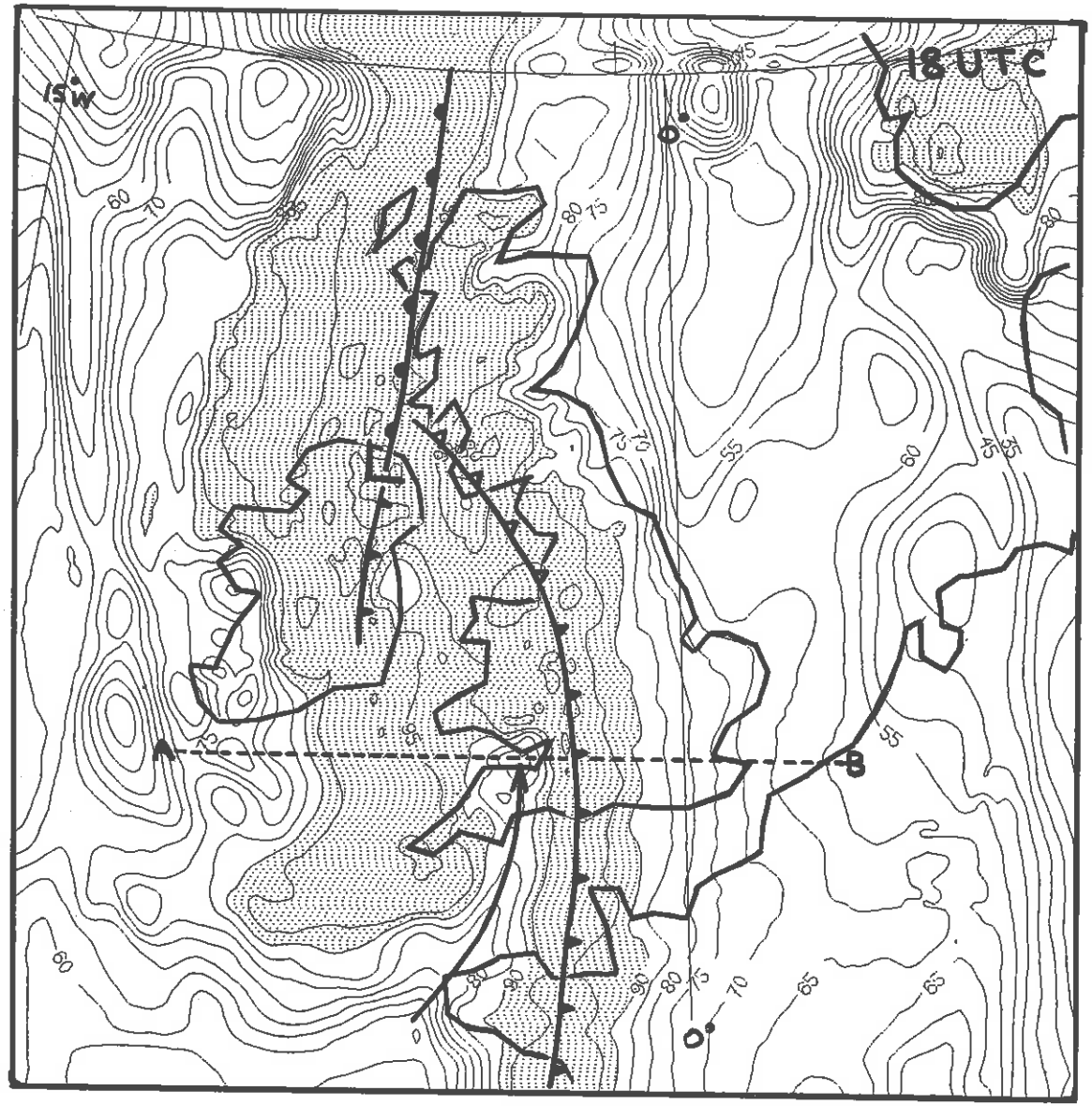

Fig 11(c)

FELATIVE HUMIDITY 650mb
VALID AT 18Z ON 24/10/1995 DAY 297 DATA TIME 18Z ON 24/10/1995

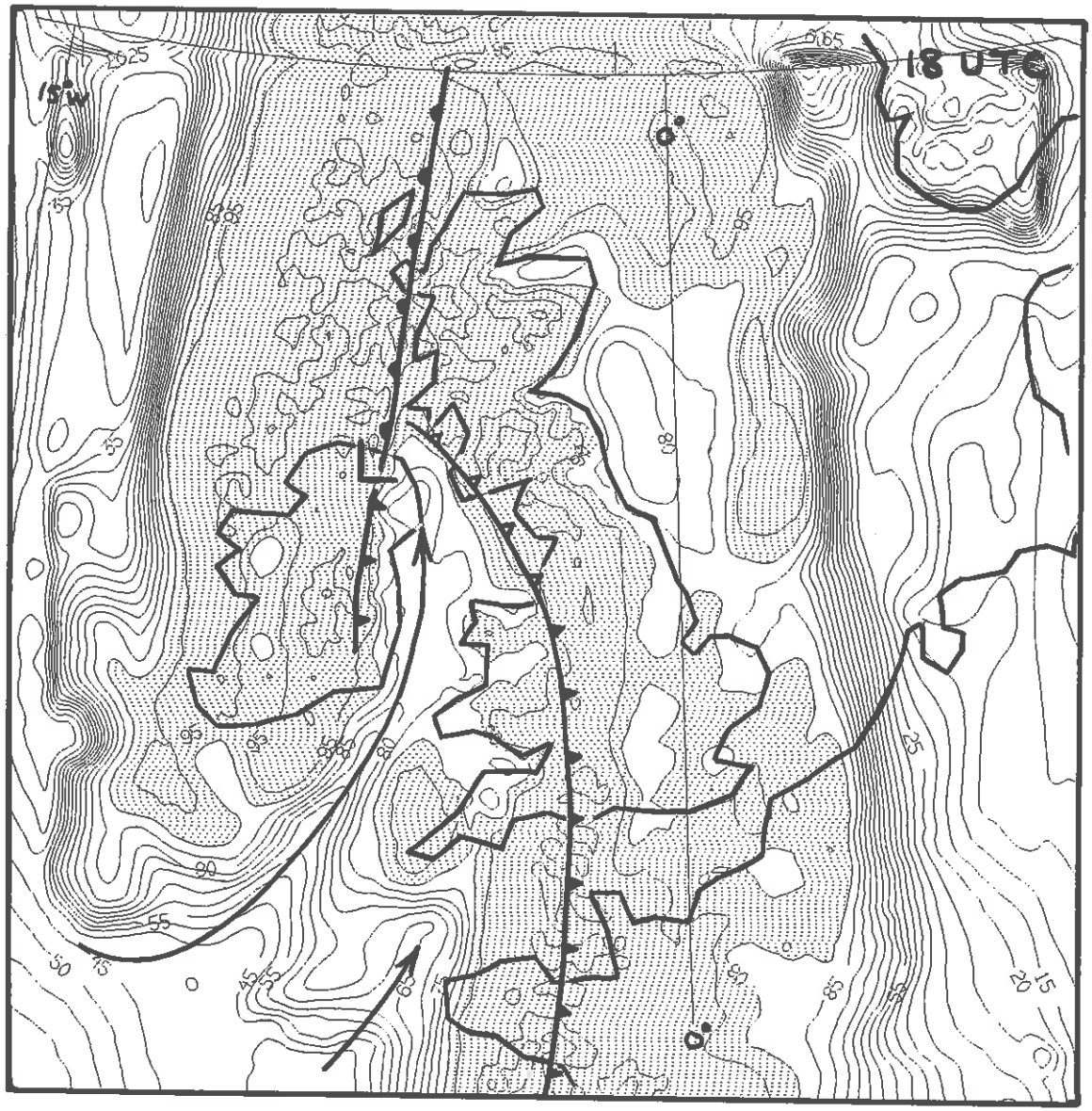

(d)

Fg 11 (d)

Figure 12

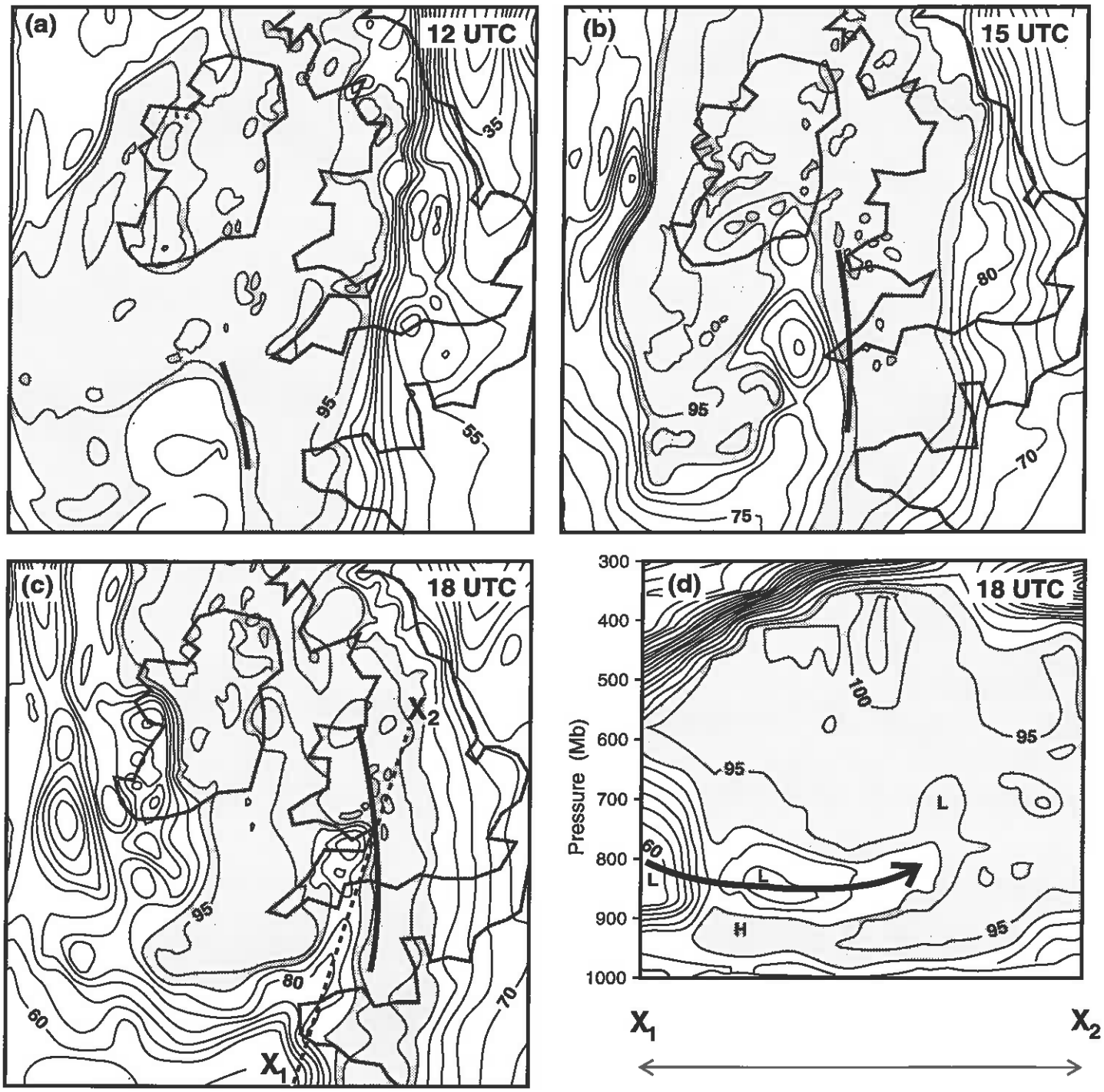
(a)
12 UTC
35
95
55
(b)
15 UTC
80
95
70
75
(c)
18 UTC
X2
95
80
60
70
X1
(d)
18 UTC
300
400
500
600
700
800
900
1000
Pressure (Mb)
100
95
95
L
60
L
L
H
95
X1
X2

Figure 13

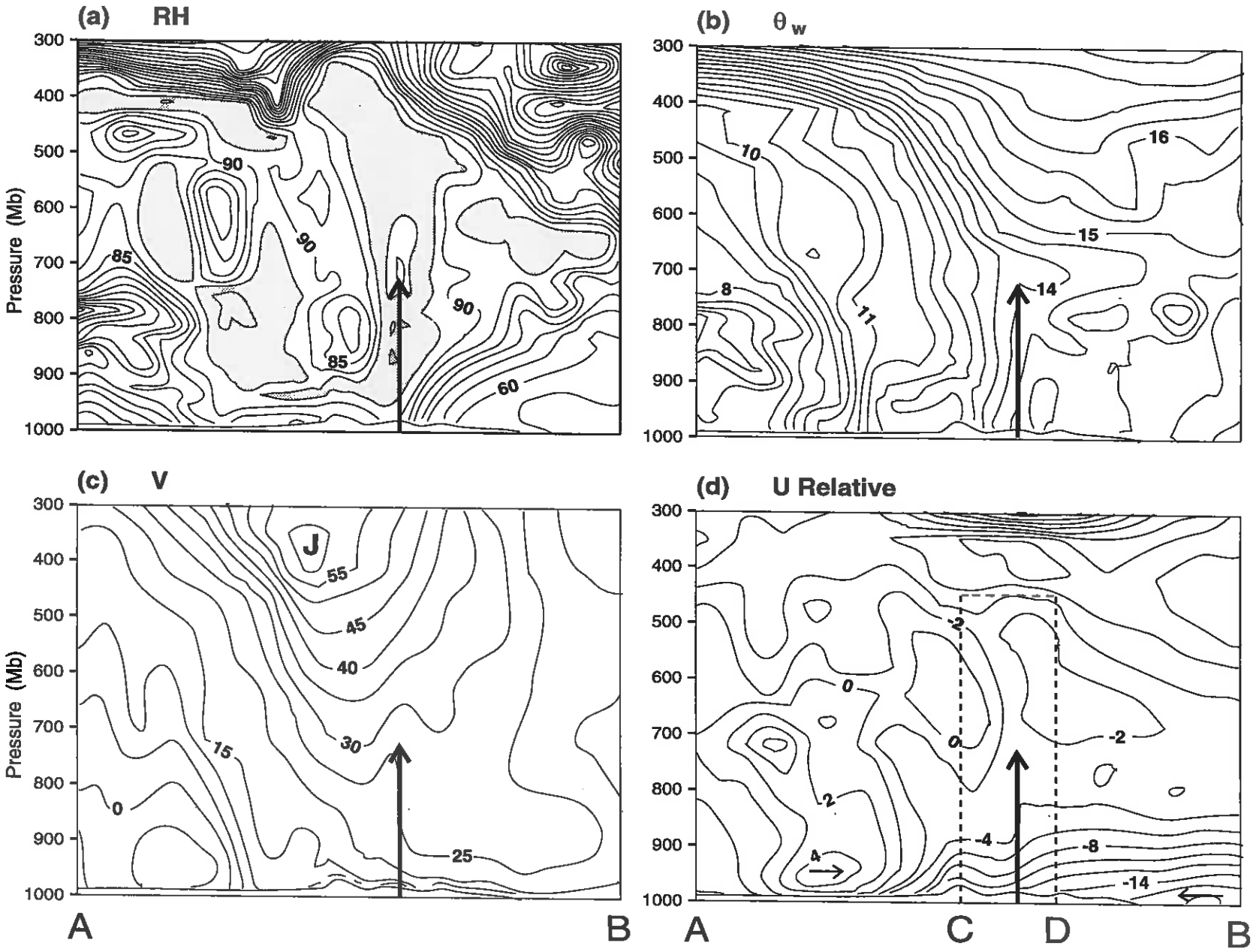
(a) RH
(b) θ w
(c) V
(d) U Relative
Pressure (Mb)
300
400
500
600
700
800
900
1000
90
85
60
10
11
8
15
16
14
J
55
45
40
30
25
0
-2
-4
-8
-14
A
B
C
D

Figure 14

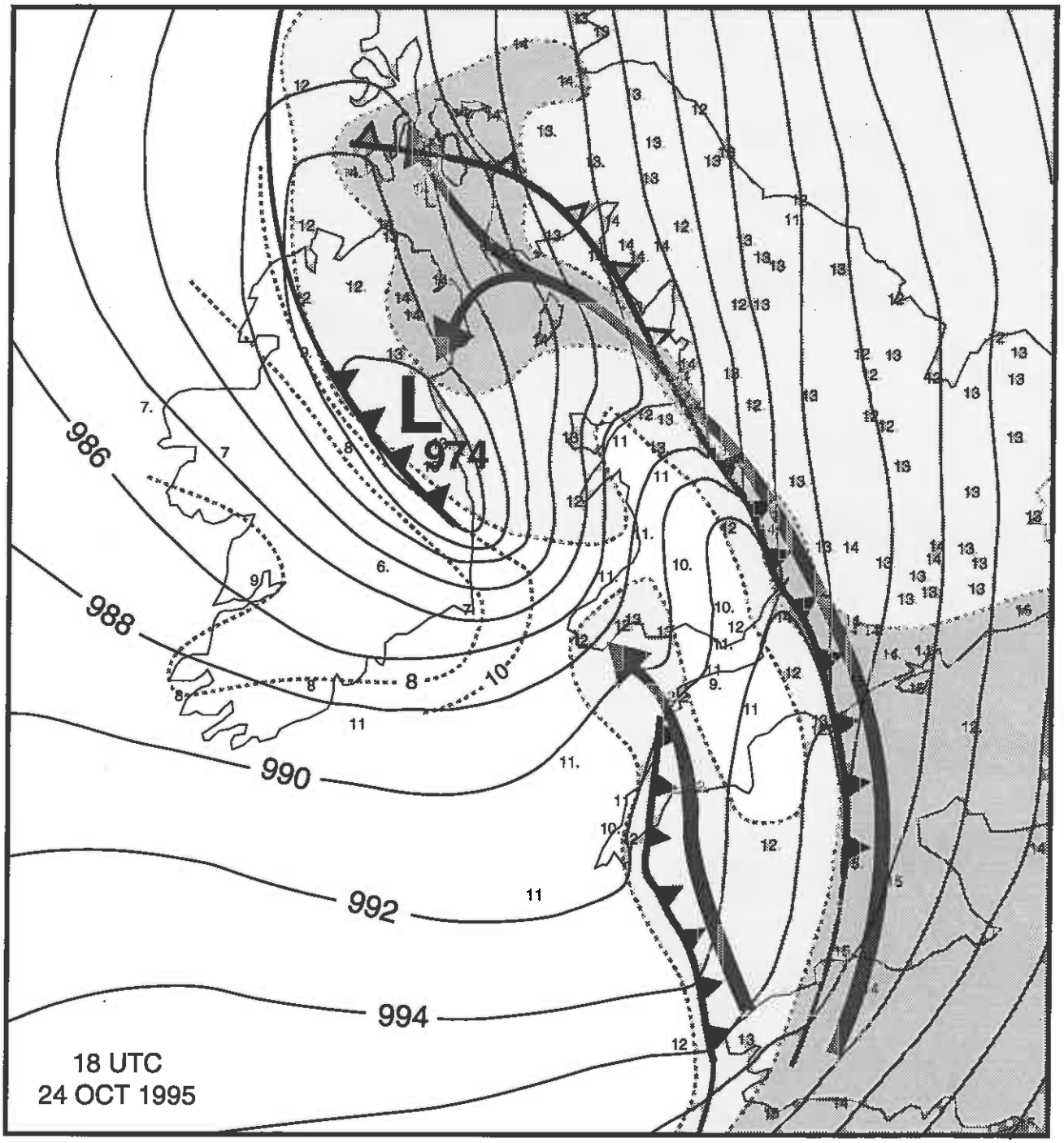

Figure 15

(a)

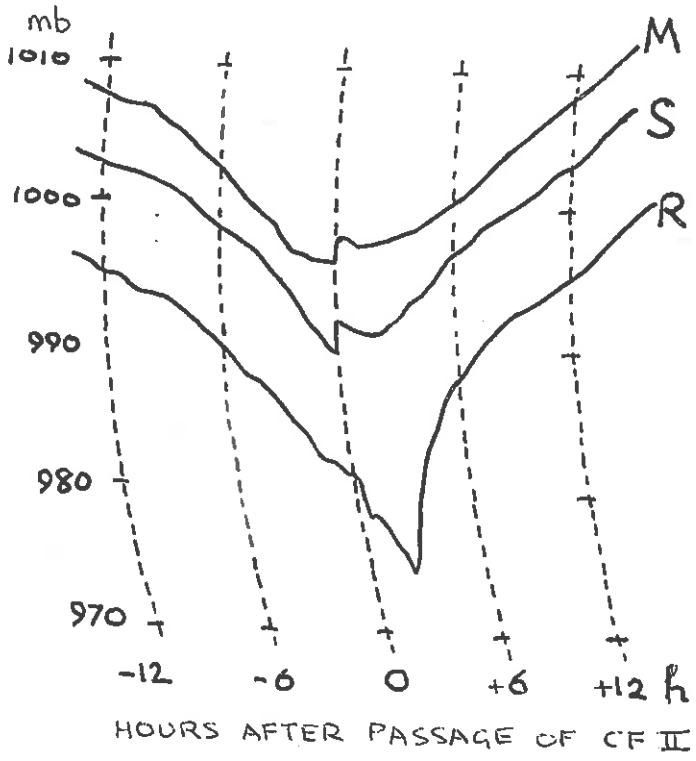
mb
1010
1000
990
980
970
M
S
R
-12
-6
0
+6
+12 h
HOURS AFTER PASSAGE OF CF II

(b)

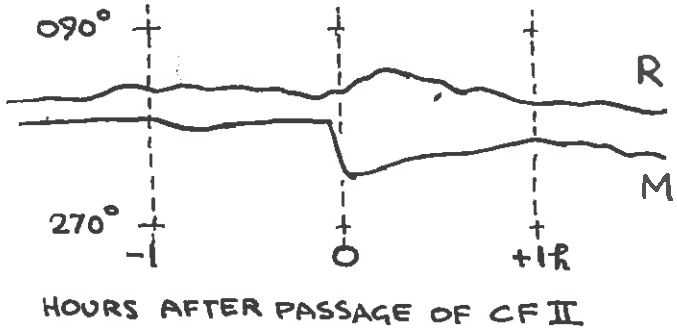
090°
270°
R
M
-1
0
+1h
HOURS AFTER PASSAGE OF CF II

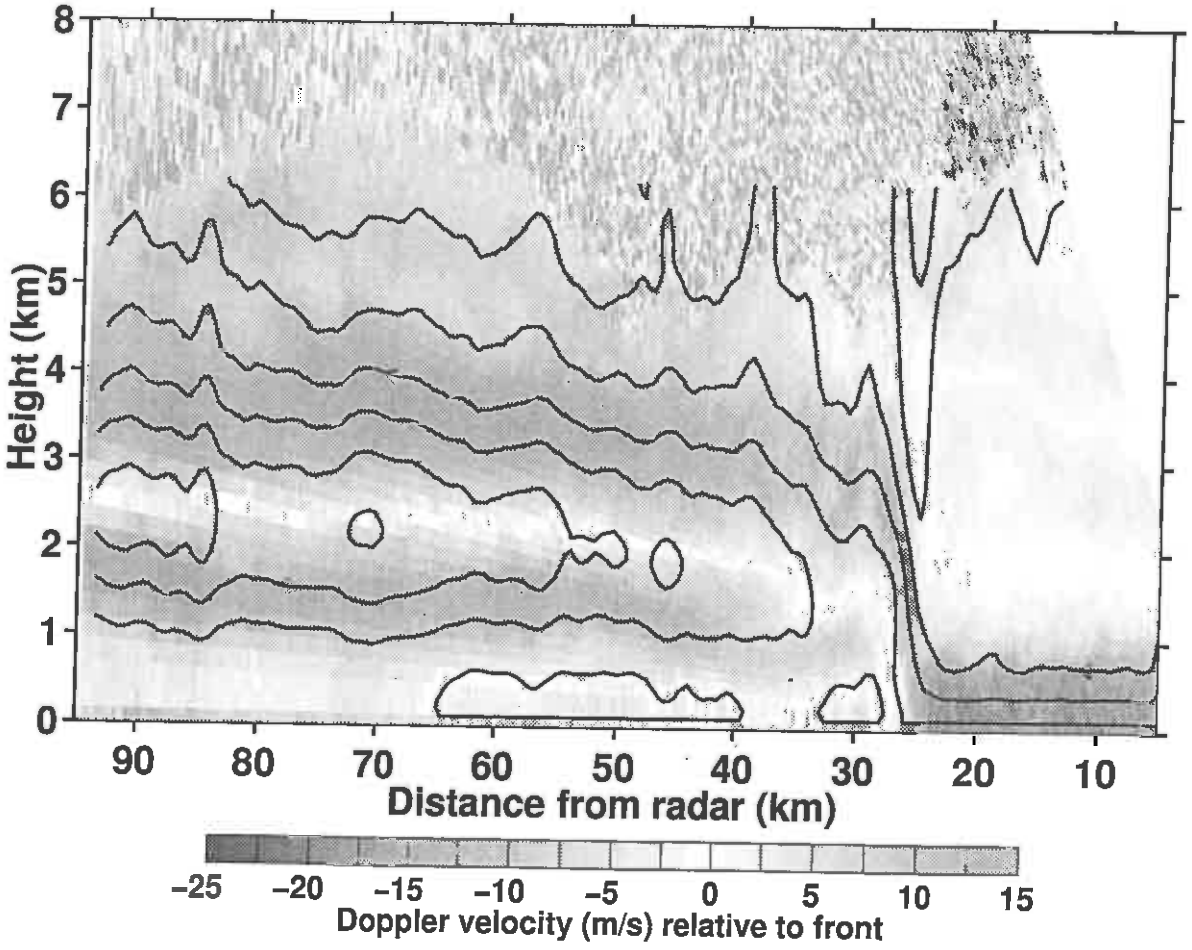
Height (km)
8
7
6
5
4
3
2
1
0
90
80
70
60
50
40
30
20
10
Distance from radar (km)
−25
−20
−15
−10
−5
0
5
10
15
Doppler velocity (m/s) relative to front

Fig. 16(a)

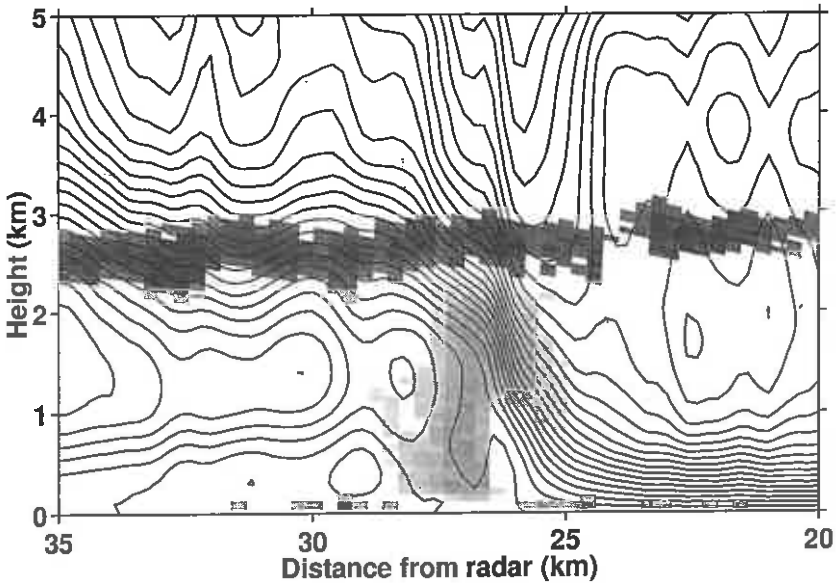
Height (km)
0
1
2
3
4
5
35
30
25
20
Distance from radar (km)

(b)

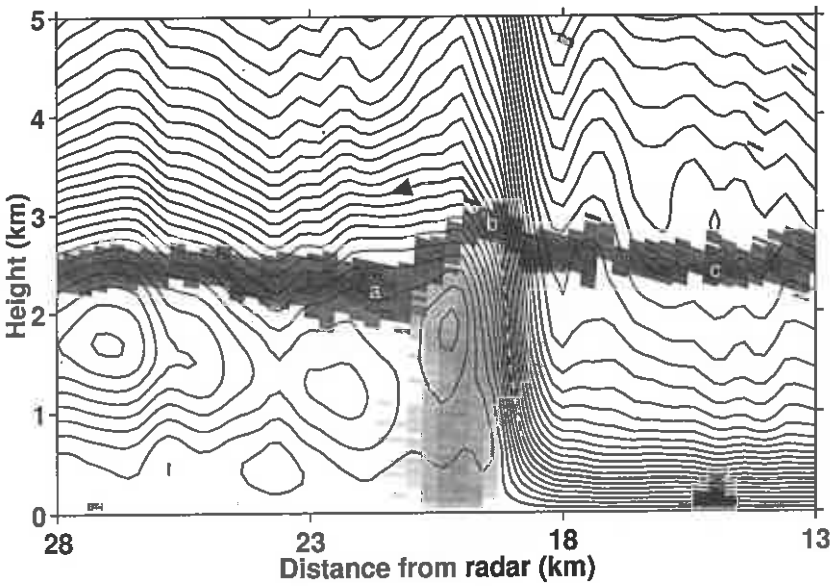
Height (km)
0
1
2
3
4
5
28
23
18
13
Distance from radar (km)

(c)

Fig 16 (b & c)

Fig 17

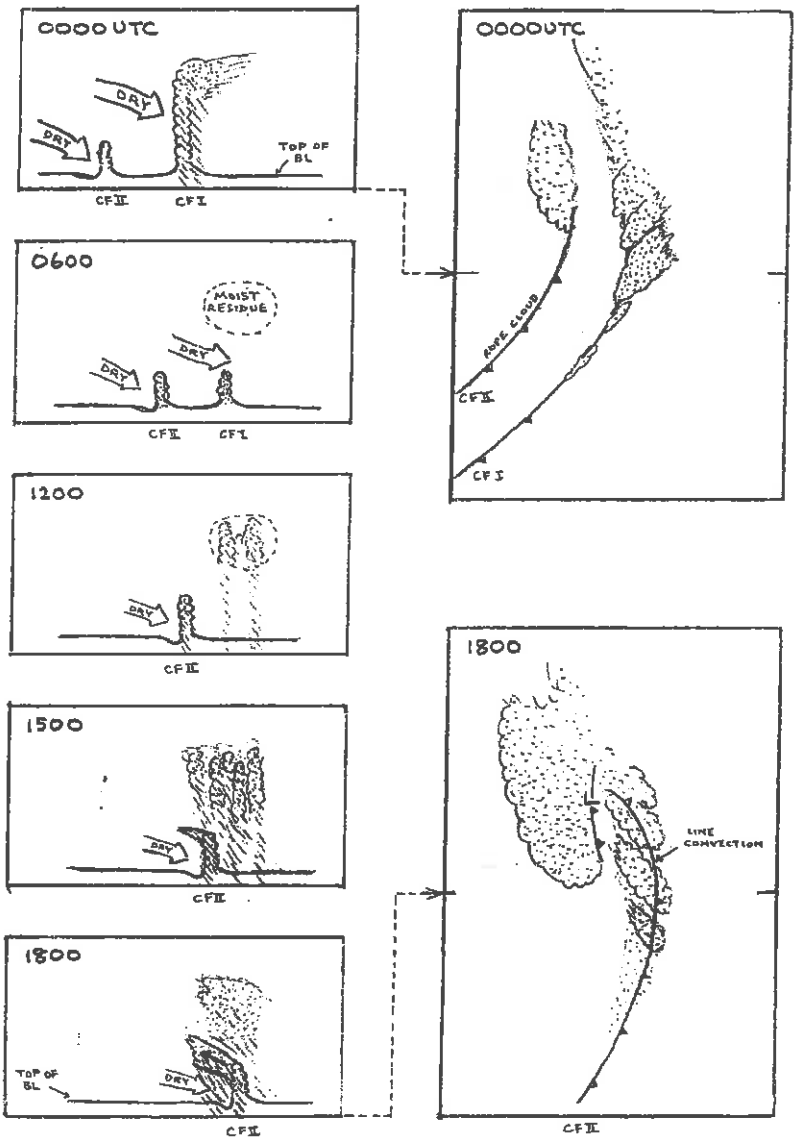
0000 UTC
DRY
DRY
TOP OF BL
CFII
CFI
0600
MOIST RESIDUE
DRY
DRY
CFII
CFI
1200
DRY
CFII
1500
DRY
CFII
1800
TOP OF BL
DRY
CFII
0000UTC
ANVIL CLOUD
CFII
CFI
1800
LINE CONVECTION
CFII

CURRENT JCMM INTERNAL REPORTS

This series of JCMM Internal Reports, initiated in 1993, contains unpublished reports and also versions of articles submitted for publication. The complete set of Internal Reports is available from the National Meteorology Library on loan, if required.

1. **Research Strategy and Programme.**
   K A Browning et al
   January 1993

2. **The GEWEX Cloud System Study (GCSS).**
   GEWEX Cloud System Science Team
   January 1993

3. **Evolution of a mesoscale upper tropospheric vorticity maximum and comma cloud from a cloud-free two-dimensional potential vorticity anomaly.**
   K A Browning
   January 1993

4. **The Global Energy and Water Cycle**
   K A Browning
   July 1993

5. **Structure of a midlatitude cyclone before occlusion.**
   K A Browning and N Roberts
   July 1993

6. **Developments in Systems and Tools for Weather Forecasting.**
   K A Browning and G Szejwach
   July 1993

7. **Diagnostic study of a narrow cold frontal rainband and severe winds associated with a stratospheric intrusion.**
   K A Browning and R Reynolds
   August 1993

8. **Survey of perceived priority issues in the parametrizations of cloud-related processes in GCMs.**
   K A Browning
   September 1993

9. **The Effect of Rain on Longwave Radiation.**
   I Dharssi
   September 1993

10. **Cloud Microphysical Processes - A Description of the Parametrization used in the Large Eddy Model.**
H Swann
July 1994

11. **An Appreciation of the Meteorological Research of Ernst Kleinschmidt.**
A J Thorpe
May 1992

12. **Potential Vorticity of Flow Along the Alps.**
A J Thorpe, H Volkert and Dietrich Heimann
August 1992

13. **The Representation of Fronts.**
A J Thorpe
January 1993

14. **A Parametrization Scheme for Symmetric Instability: Tests for an Idealised Flow.**
C S Chan and A J Thorpe
February 1993

15. **The Fronts 92 Experiment: a Quicklook Atlas.**
Edited by T D Hewson
November 1993

16. **Frontal wave stability during moist deformation frontogenesis. Part 1. Linear wave dynamics**
C H Bishop and A J Thorpe
May 1993

17. **Frontal wave stability during moist deformation frontogenesis. Part 2. The suppression of non-linear wave development.**
C H Bishop and A J Thorpe
May 1993

18. **Gravity waves in sheared ducts.**
S Monserrat and A J Thorpe
October 1993

19. **Potential Vorticity and the Electrostatics Analogy: Quasi-Geostrophic Theory.**
C Bishop and A J Thorpe
November 1993

20. **Recent Advances in the Measurement of Precipitation by Radar.**
A J Illingworth
April 1993

21. **Micro-Physique et Givrage. Cloud Microphysics and Aircraft Icing.**
A J Illingworth
May 1993

22. **Differential Phase Measurements of Precipitation.**
M Blackman and A J Illingworth
May 1993

23. **Estimation of Effective Radius of Cloud Particles from the Radar Reflectivity.**
N I Fox and A J Illingworth
May 1993

24. **A Simple Method of Dopplerising a Pulsed Magnetron Radar.**
L Hua, A J Illingworth and J Eastment
November 1993

25. **Radiation and Polar Lows.**
George C Craig
February 1994

26. **Collected preprints submitted to International Symposium on the Life Cycles of Extratropical Cyclones; Bergen, Norway, 27 June - 1 July 1994**
April 1994

27. **Convective Frontogenesis**
Douglas J Parker and Alan J Thorpe
April 1994

28. **Improved Measurement Of The Ice Water Content In Cirrus Using A Total Water Evaporator**
Philip R A Brown and Peter N Francis
April 1994

29. **Mesoscale Effects of a Dry Intrusion within a Vigorous Cyclone**
K A Browning and B W Golding
April 1994

30. **GEWEX Cloud System Study, Science Plan**
May 1994

31. **Parametrization of Momentum Transport by Convectively Generated Gravity Waves**
R Kershaw
February 1995

32. **Mesoscale Modelling Newsletter, No. 5**
May 1994

33. **Observations of the mesoscale sub-structure in the cold air of a developing frontal cyclone**
K A Browning, S A Clough, C S A Davitt, N M Roberts and T D Hewson
May 1994

34. **Longwave Radiative Forcing of a Simulated Tropical Squall Line**
Imtiaz Dharssi
July 1994

35. **On the nature of the convective circulations at a kata-cold front**
K A Browning
September 1994

36. **Collected preprints of papers submitted to the COST-75 International Seminar on Advanced Weather Radar Systems, Brussels, 20-23 September 1994**
November 1994

37. **Use of satellite imagery to diagnose events leading to frontal thunderstorms: Parts I and II of a case study**
K A Browning and N M Roberts
November 1994

38. **The role of spaceborne millimetre-wave radar in the global monitoring of ice cloud**
P R A Brown, A J Illingworth, A J Heymsfield, G M McFarquhar, K A Browning and M Gosset
December 1994

39. **Potential Vorticity Inversion**
Michal Ziemianski
October 1994

40. **Theory of mature tropical cyclones; A comparison between Kleinschmidt (1951) and Emanual (1986)**
Suzanne L Gray
December 1994

41. **Dispersion and removal of pollutants during the passage of an atmospheric frontal system**
N R Gimson
December 1994

42. **The role of snow sublimation in frontogenesis**
D J Parker and A J Thorpe
December 1994

43. **Potential vorticity and the electrostatics Analogy: Ertel-Rossby formulation**
A J Thorpe and C H Bishop
December 1994

44. **Mesoscale aspects of extratropical cyclones: an observational perspective**
K A Browning
January 1995

45. **A Polar Low Outbreak: Evolution and Mesoscale Structures**
T D Hewson, G C Craig and C Claud
February 1995

46. **Generation of near-surface gusts by deep convection**
K Nakamura and R Kershaw
April 1995

47. **Attribution concepts applied to the omega equation**
S A Clough, C S A Davitt and A J Thorpe
June 1995

48 **Parametrization of mixed-phase cloud and precipitation**
Susan P Ballard and M Gerard Hutchinson
June 1995

49 **Short-range forecasting of stratocumulus: Initialization V Prediction**
Susan P Ballard, Simon D Jackson and B Macpherson
June 1995

50 **Contributions of the JCMM/Dept of Meteorology Radar Group to the 27th AMS Radar Meteorology Conference, Vail October 1995**
June 1995

51 **Cold pools in shear**
Douglas J Parker
September 1995

52 **High-resolution analysis of frontal fracture**
K A Browning, S P Ballard and C S A Davitt
September 1995

53 **The Albedo of Broken Cloud Fields: Calculations using a modified two stream radiation code**
Imtiaz Dharssi and Roy Kershaw
October 1995

54 **Parametrization of momentum transport by convection. I: Theory and cloud modelling results**
R Kershaw and D Gregory
November 1995

55 **Variation of frontal structure along a cold front**
K A Browning and N M Roberts
November 1995

56 **Secondary Frontal Waves**
Douglas Parker
December 1995

57 **Objective Fronts**
T D Hewson
March 1996

58 **Mesoscale analysis of the activation of a cold front during cyclogenesis**
K A Browning, N M Roberts and A J Illingworth
June 1996

Met Office Joint Centre for Mesoscale Meteorology Department of Meteorology
University of Reading PO Box 243 Reading RG6 6BB United Kingdom
Tel: +44 (0)118 931 8425 Fax: +44 (0)118 931 8791
www.metoffice.com